2-14-2014

EXPLORATION OF TM-NX ORR ELECTROCATALYSTS FROM FIRST PRINCIPLE CALCULATIONS

Sadia Afrin Kabir

Follow this and additional works at: https://digitalrepository.unm.edu/cbe_etds

Recommended Citation

Sadia Afrin Kabir
Candidate

Chemical and Nuclear Engineering
Department

This thesis is approved, and it is acceptable in quality and form for publication:

Approved by the Thesis Committee:

Plamen Atanassov, Chairperson

Boris Kiefer

Kateryna Artyushkova

Dimiter N. Petsev

EXPLORATION OF TM-N$_X$ ORR ELECTROCATALYSTS FROM FIRST PRINCIPLE CALCULATIONS

BY

SADIA AFRIN KABIR

B.E (HONS) CHEMICAL ENGINEERING

THESIS

Submitted in Partial Fulfillment of the
Requirements for the Degree of

Master of Science

Chemical Engineering

The University of New Mexico
Albuquerque, New Mexico

December, 2013

DEDICATION

To Ammu and Abbu

ACKNOWLEDGEMENTS

EXPLORATION OF TM-N$_X$ ORR ELECTROCATALYSTS FROM FIRST PRINCIPLE CALCULATIONS

by

Sadia Afrin Kabir

B.E (Hons), Chemical Engineering, Bits Pilani - Dubai, 2011
M.S., Chemical Engineering, University of New Mexico, 2013

ABSTRACT

Fuel Cells are promising candidates for the energy conversion technologies in particular for non-stationary applications. However, current fuel cells rely on rare and expensive Platinum catalysts and the power generation is limited by the sluggish oxygen reduction reaction (ORR) at the cathode. An interesting alternative material set which continues to attract significant attention are TM-N$_x$ (TM = Fe, Co, x = 2 - 4) based non-PGM electrocatalysts where the defect motifs are embedded in a carbon matrix during pyrolysis. By studying the material properties of individual defects we can determine how the chemistry and morphology of these TM-N$_x$ motifs are interdependent.

Additional focus will also be on XPS characterization for the identification of the nature of proposed catalytic site(s). Although XPS is a widely used experimental technique for this purpose, the unique identification of structural motifs from XPS observations alone remains challenging.

First-principles computations can provide us with the missing link by predicting core-level shifts for candidate defect motifs. This ability enables us to establish structure/property relationships directly and provides us with information that is critical for the detailed interpretation of XPS spectra. The incentive of this research thesis resides in the understanding of the electrochemical performance and energetics of these TM-N_x catalysts and the quest for the design of suitable catalysts with improved performance.

TABLE OF CONTENTS

LIST OF FIGURES

LIST OF TABLES

Chapter 1

Introduction

One of the most significant challenges of the 21st century is expected to be energy production. This is mainly due to the increasing rate at which natural resources and petroleum reserves are being depleted, an accelerating population growth and the goal to constraint carbon emissions may prevent us from burning those fossil fuels that remain available.[1,2] It is only a matter of time before the oil and natural gas prices start increasing, and this will make renewable energy technologies competitive in the future.[3] Thus developing sustainable energy technologies like Proton Exchange Membrane Fuel Cells (PEMFC) may play a significant role in the production of clean energy or provide at least a partial solution to the increasing societal demand of non-stationary energy.

Among all the other renewable alternatives, PEMFCs have received the widest attention over the recent few decades as an environmentally friendly technology. The coupling of hydrogen technology to renewable energies can be particularly productive. As opposed to batteries, PEMFC's technology is facilitated to store the fuel in a separately connected isolated tank, where the fuel can be supplied on demand.[4] The most important advantage of fuel cells is their high efficiency, which in contrast to combustion engines is not limited by the 2nd law of thermodynamics. This is of particular interest at low loads and makes low-temperature fuel cells desirable for urban traffic. This advantage is reinforced by the zero tailpipe emission of hydrogen fed fuel cells. Due to their low temperatures and high power densities, fuel cells have become a promising candidate for the next generation power source.[5,6]

Limitations of Platinum Based Fuel Cells

Currently, platinum group metals (PGMs) are regarded as the most active cathode catalysts for oxygen reduction reaction (ORR) in fuel cells. However, Platinum based fuel cells are comparatively expensive and its high costs[7] are posing a significant barrier by deterring the further commercialization of PEMFCs.[8] At present, the most expensive[9] component is the polymer membrane at a price of 500\$/m^2 (Nafion from Dupont).[10] Platinum also accounts for up to half of the fuel cell cost.[11,1,12]

Other key issues that are impeding the final application of fuel cells are the sluggish oxygen-reduction reaction at the cathode that lead to high voltage losses as the platinum content is 5-10 times larger in the cathode, making oxygen reduction reaction slower than hydrogen oxygenation at the anode. PGM catalysts also tend to have stability issues, due to the agglomeration and dissolution of Platinum particles into the electrolyte.[13]

Therefore, to scale up this technology, it has become important to develop more cost-effective non-PGM based fuel cell catalysts that reduce or eliminate PGMs from the catalyst design,[1] especially with the 9\$/kW Membrane-Electrode-Assembly target set by the DOE for transportation in 2017.[12] Hence alternative materials to PGM electrocatalysts need to be explored with research aimed at looking for alternative materials that are cheaper and could yet perform better or equivalent to the Platinum standard and replace it with significantly more abundant transition metals such as Fe, Co, Cu, Mn, Mo for multielectron transfer catalysts, thereby making PEMFCs commercially feasible for applications other than in niche markets.[14]

Alternatives: Non-PGM TM-N$_x$ Electrocatalysts

The primary objective of electro-catalytic research has been noble-metal-free ORR electrocatalysts that are active and durable in acid electrolytes.[15] Many efforts have been made to reduce the cost of electrocatalysts by substituting the Platinum cathode with less expensive materials.[3,16,17] Among those, alloys of Platinum and transition metals such as Fe, Co, Ni, Cr, etc. are generally used due to their abundance and economical manufacturing costs.[18] Of these transition metals, iron and cobalt-based nanostructures on Nitrogen functionalized[19] mesoporous carbons are beginning to emerge as possible contenders for future commercial PEMFC systems due their excellent conductivity, high surface area and the cheap manufacturing costs of the carbon support.[7,20,21]

Studies show that the use of transition metals in catalysts in the form of metal complexes such as chalcogenides,[22] transition metal oxides or nitrides and macrocycles have reasonable electro catalytic activity.[7,23,24] Recent experimental studies have shown excellent ORR activity in TM–N$_x$/C (TM = Fe, Co)[1], where the TM is usually cobalt or iron, embedded in a Nitrogen containing Carbon support (Fig 1).[25]
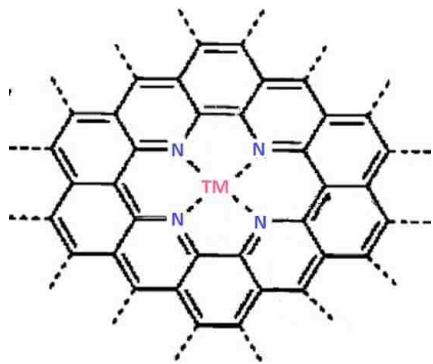
Fig 1 : A TM-N$_4$ defect embedded in a Carbon matrix.[7]

Synthesis, ORR Mechanisms and Nature of the Active Site

There are quite a few well known alternative approaches available for the preparation of TM/N$_x$-C electrocatalysts that are being practiced at present. The requirements for synthesizing nitrogen-doped carbon-based non-precious metal are namely (i) a transition metal, (ii) surface nitrogen and (iii) carbon.[18] Two pyrolysis synthesis routes have been widely adopted so far :

1) Pyrolysis of a Carbon supported metal salt in a Nitrogen-rich atmosphere (ammonia, acetonitrile)

2) Pyrolysis of a Carbon supported Nitrogen-containing polymer in the presence of a metal salt.[26]

Transition metal macrocycles catalysts are generally prepared by impregnation of a transition metal N$_4$-chelate[27] precursor onto black Carbon. This is followed with more heat treatment under inert atmosphere as reported by Jaouen et al.[28,29]

Substantial attention has also been given to the oxygen reduction reaction (ORR) at the cathode, which at present limits the overall performance of a fuel cell as it seems to be responsible for the majority of the voltage losses occurring in a fuel cell.[30] Recent studies have shown that the overall reduction kinetics and reaction pathways are affected by molecular chemiabsorption and the chemical nature of bonding of the adsorbed oxygen to the catalyst surface.[31] Therefore, a better understanding of the active site morphology and the reaction steps that occur on the moieties is needed if transition metal catalysts are to replace platinum based materials in PEM fuel cells.[7]

4

The reduction of the oxygen molecule is known to proceed through either of the two main routes in an acidic solution:

1) The direct 4-electron reduction reaction to produce water:

$O_2 + 2H^+ + 4e^- \leftrightarrow 2H_2O$ $\qquad E_0 = 1.229V$ (1)

2) The parallel pathway, the 2x2 electron reduction reaction to produce hydrogen peroxide, which can undergo further reaction to produce water.

$O_2 + 2H^+ + 2e^- \leftrightarrow 4H_2O_2$ $\qquad E_0 = 0.695V$ (2)

$H_2O_2 + 2H^+ + 2e^- \leftrightarrow 4H_2O$ $\qquad E_0 = 1.76V$ (3)[7]
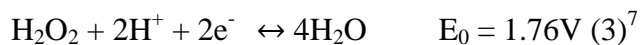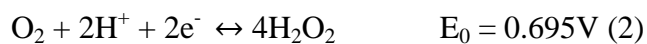
The chosen catalyst material determines the extent of the reaction. H_2O_2 produced in two-electron process is the primary cause of the degradation of the catalytic site, causing poor stability (Fig 2).[18]
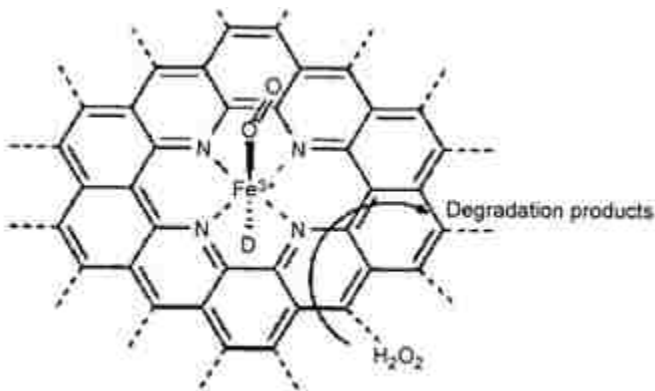
Fig 2 : Proposed model for the ORR reaction taking place on a TM-N$_x$ active site.[5]

A catalyst for ORR needs to be designed in such a way that it favors the reduction of oxygen molecules to water through the four-electron route instead of the two-electron route that produces hydrogen peroxide and degrades the catalyst. .[18] There's another group of Fe/Co-N_x-C catalysts known as bifunctional catalysts which are typically heterogeneous and consist of many different moieties.[32] In these catalysts the 2x2 ORR occurs in two electrochemically distinct steps on two physically and chemically distinct active sites, where once the oxygen molecule is adsorbed onto the catalytic site, it either follows the $2e^-$ pathway to produce peroxide or the $4e^-$ pathway to produce water. The reaction intermediate hydrogen peroxide is either (i) adsorbed on the surface, (ii) reduced to water, or (iii) chemically decomposed to form water and oxygen.[33] Each of these reactions occur on either a nitrogen-functionalized-metal (TM-N_x) defect[34], metal-oxide or the graphitic defect respectively.[35]

The nature of the active site/sites of non-PGM oxygen reduction reaction (ORR) electrocatalysts has been debated for the past 50 years and is still unclear.[36] Most researchers have proposed that TM-N_x bound to the carbon matrix plays a crucial role in ORR whereas others have suggested that it is nitrogen alone that is responsible for ORR.[37] However, based on Time of Flight Secondary Ion Mass Spectrometry (ToF SIMS) studies of Fe/N_x-C catalysts conducted previously by many groups, it is believed by most that the metal is an integral part of the design principles of the most ORR-active electrocatalysts.[12,34,38]

Activity and Stability

The performance of a catalyst (activity, stability, and selectivity) is directly related to catalyst structure, which varies greatly according to the catalyst preparation conditions, metal precursors used during synthesis, ligand structure, carbon support and heat treatment temperatures.[37] This can be attributed to reduced production of hydrogen peroxide during the ORR process, which attacks the active site.[18] Among them, Fe and Co centers have been shown to have the highest observed activity, with Co being more active than Fe in acidic media.[39]

It has also been shown that the ORR activity of the catalysts increase significantly after heat-treatment in the presence of 0.2 wt. % Fe.[37,40,41] It has been established that their ORR-activity is proportional to and governed by (i) the transition metal content, (ii) the post-pyrolysis microporous surface area and (iii) the concentration of Nitrogen functionalities.[12,18,42] It has also been shown that the stability of nitrogen functionalized transition metal electrocatalysts can be greatly improved by using heat-treatment.[42,43]

Understanding the interdependencies of chemistry and morphology is only possible by studying individual building blocks that are present in electrocatalysts with various levels of defects introduced. Thus, theory can be used to design materials with desired properties and complement experiments.

Chapter 2

First Principle Calculations of TM-N$_x$ ORR Electrocatalysts

While computers are getting cheaper and more powerful, experiments are becoming more expensive to perform. With computer simulations offering ever more accuracy, it is only reasonable to assume that, provided with good computing resources, at some point simulating experimental measurements should become cheaper than the experiment itself. This has already occurred in many branches of science and engineering where first-principles electronic structure calculations are used to describe both bulk and molecular and atomic systems.[44]

The following chapters will be focused in the understanding of the electrochemical performance of the cathode in the polymer electrolyte fuel cell and energetics of TM-N$_x$ catalysts and the quest for the design of suitable catalysts with improved performance using first principle density functional theory (DFT) calculations.
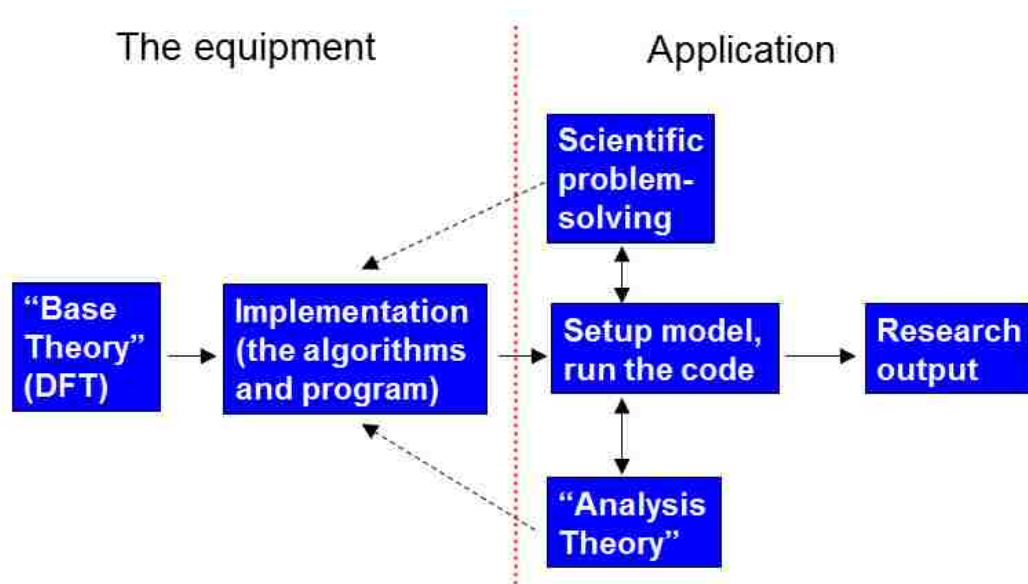
Fig 3 : Computational pathway (Introduction to Computer Simulation: Edinburgh, May 2010)

Density Functional Theory (DFT)

For the past 30 years DFT has been the dominant method for the simulation of many-electron systems. It has also been implemented in recent years by quantum chemists and is now extensively used for the simulation of energy surfaces in molecules, predicting and verifying properties.[45] Density functional theory (DFT) is presently the most successful (and also the most promising) approach to compute the electronic structure of matter due to its accurate predictive powers of computing a great variety of molecular properties and interpreting experimental results.[46,47]

The starting point of density functional theory is the many electron Schrödinger wave equation (1) ▮▮▮▮▮▮[48], where H is the Hamiltonian, Ψ is the many electron wave function and E is the energy of the system. Quantum mechanically, equation (1) is simply an eigenvalue problem and the energies may be solved inserting the Hamiltonian operator. The Hamiltonian encompasses all interaction within the system: ▮▮▮▮▮▮, where T is the kinetic energy, V is the external potential and U is the electron-electron interaction.[49,50] In materials simulation the external potential of interest is simply the interaction of the electrons with the atomic nuclei. The lowest energy eigenvalue, E_0, is the ground state energy and (Ψ_2) is the probability density of finding an electron in a volume element of interest.[51] The Hamiltonian operator is used to determine the electronic ground state by solving the Kohn-Sham equations:

$$\left[-\frac{1}{2}\nabla_i^2 + V_i^{KS}[n(\vec{r})] \right]\psi_i(\vec{r}) = \lambda_i\psi_i(\vec{r})$$

where i labels each particle in the system, V_i^{KS} is the potential felt by particle i due to the presence of the other electrons.[52,53]

9

The transition from the many electron problem (Eqn 1) to the one-electron like Kohn-Sham equations deserves a few comments: (i) The intractable many electron problem has been mapped onto an in principle equivalent and exact one electron problem; (ii) The Kohn-Sham equations depends on the charge density and the coordinates of a single electron rather than the coordinates of all electrons. That is to say that the electron moves in the mean potential due to the presence of the other electrons and can be considered as a mean-field approximation; (iii) The theory is in principle exact and can be applied to material of arbitrary complexity. This shows that DFT has the predictive power that is needed for materials exploration and design; (iv) Looking at the Kohn-Sham equations two immediate criticisms are apparent: the lack of the Pauli exclusion principle and the effect of correlations between electrons. However, both effects are included by the introduction of an exchange-correlation potential in the effective $V^{KS}[n(r)]$ potential.

While DFT is, in principle exact,[52] it relies on the unknown parameterization of the exact exchange correlation potential. For this reason, many different parameterizations of the exchange correlation potential exist. LDA (Local Density Approximation)[54,55] is the simplest form and only depends on the charge density, followed by GGA (Generalized Gradient Approximation) which depends on the charge density and its gradient. These are the most commonly used approximations in use today. However, improvements of the GGA such as meta-functionals have been introduced by including the second derivatives of the charge density.[56] Other strategies include the re-introduction of the exact exchange for example in HSE03 and HSE06 which are screen hybrid density functionals.[57]

Solving the Kohn-Sham equations provides a relatively efficient and unbiased tool to compute material properties of bulk materials, surfaces, and molecules. In the present research we use DFT to compute (i) experimentally accessible properties of candidate $TM\text{-}N_x$ motifs (ii) structure/property relationships (iii) charge density, wave functions, band energies, and equilibrium structure, (iv) magnetism and the electronic spin of Fe in particular (v) energetics which gives valuable insights into defect formation energies and their stability and, (vi) XPS core level shifts for different types of defects.

Objectives of Theoretical Modeling

The present DFT study will explore the role of magnetism on the ORR activity of graphitic $TM-N_x/C$ (x = 2 - 4) based self-assembled carbon supported electrocatalysts. The TMs in $TM-N_x/C$ electrocatalysts are often ferromagnetic transition metals, such as Fe, Co, or Ni. This implies that the magnetic state of the catalyst may provide an additional degree of freedom for catalyst design.[12] The first-principles computations are performed to determine the ground state energies and magnetic properties of $TM-N_x/C$ defects. The practical objective is then to model, preprocess and generate $TM-N_x$ defect motifs using VASP. Each of the motifs (x = 2...4) will then be analyzed for their thermodynamic stability, magnetism, with particular focus on their core-level binding energies and correlations with XPS observations. In particular, we will be focusing on our recent efforts to understanding and discuss the geometry and chemistry dependence of N1s, Fe2p, and C1s core level shifts and compare different computational protocols where possible to experimental observations which will be critical for the detailed interpretation of XPS spectra.

Preprocessing and Visualization

CrystalMaker and Jmol: The input structures were first preprocessed, generated and visualized using Jmol and CrystalMaker, both of which are software packages used for displaying and manipulating chemical structures.

VASP: The Vienna *ab-initio* Simulation Package was used to determine the electronic ground state of the defects and reference structures. It is a computer program for atomic scale materials modeling, e.g. electronic structure calculations and quantum-mechanical molecular dynamics, from first principles. It computes an approximate solution to the many-body Schrödinger equation, either within density functional theory (DFT) and determines the electronic ground state from solving the Kohn-Sham equations.

Computation Method

The spin-polarized density functional theory (DFT)[58,52,59] computations were performed using the parallelized 3D periodic Vienna *ab-initio* Simulation Package (VASP) code.[60] In VASP, central quantities, like the one-electron orbitals, the electronic charge density, and the local potential are expressed in plane wave basis sets. In the present calculations, the interaction between the ions and valence electrons and nuclei-electron interaction is described by the projector augmented wave (PAW) method.[61,62] The generalized gradient approximation (GGA) as parameterized by Perdew, Burke and Ernzerhof (PBE) was used to describe the electronic exchange and correlation effects.[63]

A plane wave energy cutoff of E_{cut} = 800 eV was used throughout the computations for optimizing the geometry as well as a 4x4x1 Monkhorst–Pack grid [64] which leads to converged solutions of the Kohn-Sham equations. The artificial interactions between the sheet and its periodic images were minimized by separating slab and its perpendicular images through a vacuum layer of 14 Å thickness. Non-magnetic Carbon atoms were chosen on the basis of test calculations that showed that this setting does not affect the magnetic state of the relaxed structure.[30] During the calculations all electronic and structural degrees of freedom were allowed to relax simultaneously while the shape of the simulation cell was held fixed at the values as obtained from the DFT-optimized parameters for defect-free graphene.

Generating the Defects

All systems were modeled as three-dimensional periodic structures. Monolayer graphene served as a model system for the Carbon support in self-assembled TM$-$N$_x$/C ORR electrocatalysts. The Carbon support in the catalyst was modeled as a 4 x 4 graphene orthorhombic supercell with lattice parameters a = 9.842 Å, b = 8.524 Å (containing 32 atoms) subjected to periodic boundary conditions.[30]

The graphene sheet is functionalized with a transition metal and Nitrogen atoms which is our proposed active site is embedded in the Carbon matrix. The in-plane defects were generated by first removing the appropriate number of Carbon atoms from graphene and then substituting it with Nitrogen (x > 0), and finally adding add one TM in the center of each remaining vacancy (TM$-$N$_x$ defect) as needed (Fig 4).

Modeling consistently shows that the TM-N$_x$ motifs are planar

a)   b)   c)
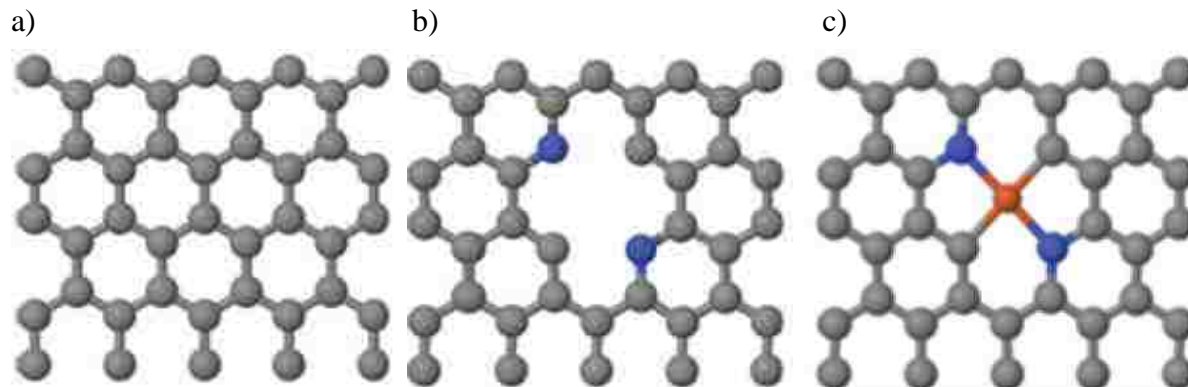
Fig 4 : Graphene configurations : a)Reference structure b)Pyridinic N$_2$-Graphene c)TM-N$_2$ defect [65]

Magnetism in TM-N$_x$ Electrocatalysts

Graphene is a resourceful material with applications in areas ranging from energy production to mainstream electronic devices and bio-sensors.[66] The versatility and resourcefulness of graphene can be attributed to its electronic structure, at least to some degree, as the electronic and magnetic properties of graphene can easily be altered and modified through a combination of transition-metal and Nitrogen in a decoration of vacancies.[67] Doping with Nitrogen has been shown to be an effective chemical route to tune the electronic properties of Carbon nanostructures.[67,68] Functionalizing graphene with Nitrogen can be used to tailor the magnetic and electronic properties of graphene and take advantage of its unique physical and chemical properties.[20,65] Ferromagnetic transition metals (TMs) such as Co and Fe are attractive modifiers for graphene because they allow the magnetic moment to be increased significantly beyond that obtained in the Carbon-only or Nitrogen doped case.[65] If the catalytic sites are magnetic, additional analysis techniques such as magnetic Mössbauer measurements may assist us in the unique identification of the geometry, chemistry, and location of catalytically active sites.[69]
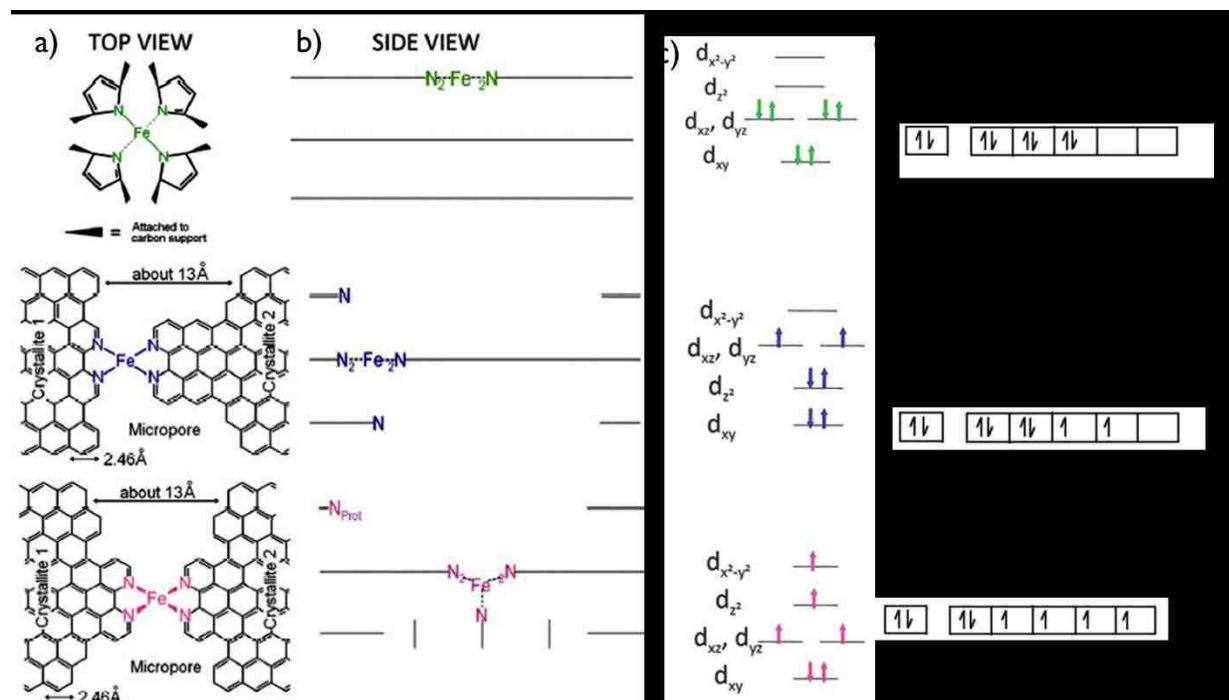
Fig 5 : Characterization of different spin states of Fe in the catalyst a) Top view b) Side view c) D orbitals d) Spin states.[12]

Crystal field theory suggests that many TM's adopt a 6-fold coordination rather than a 4-fold coordination.[70] This is also supported by recent Mössbauer experiments which support non-planar TM-N_x defect motifs.[12] The use of magnetic measurements may provide new and complementary insights into the location, chemistry, and geometry of ORR active sites at least in Carbon-supported TM−N_x electrocatalysts.[30]

Fe Mössbauer spectroscopy has been used to differentiate various Fe-sites of similar structure but dissimilar oxidation and/or spin states.[12] Jaouen et al. have shown a correlation between Fe spin state and ORR activity. This study also emphasized the possible role of the half occupied dz^2 orbital for ORR, which is reasonable in the sense that the dz^2 is oriented out of plane and hence may provide a prime catalytic site for electrocatalysis (Fig 5).

Furthermore, values obtained from Mössbauer spectroscopy resemble those of "picket-fence" porphyrins, which have high spin states (S = 2) caused by the positioning of the iron out of the N_4-plane.[12,71] Therefore, coordinating the Fe-N_4 in-plane defect with an additional N atom perpendicularly may induce a high spin state with 4 unpaired electrons.

Iron has an outer shell electronic configuration of *$4s^2 3d^6$*, with 4 unpaired electrons when it is in a high spin state. This state is important for achieving high ORR activity in Fe-N_4 catalysts and it has the highest probability to pair with O_2 and reduce it, hence improving ORR activity. π-electrons may also affect geometry and chemistry of the proposed active sites and their interactions might promote a high-spin state in Fe. The increased stability in the presence of the defects associated with TMs can be attributed to the reduced electrostatic repulsion between Nitrogen lone-pair electrons due to the hybridization between N and the TM.[65]

High Spin Configuration and Relative Sheet Separation

A possible key for reconciling experiment and theory is the notion that the Nitrogen content is higher than needed to form the defects. Previous work has shown that we only find low spin and intermediate spin state in *single* layer TM-N_x defects.[65] However, excess Nitrogen may assist in the formation of out-of-plane position of the transition metal in a bilayer system. There is a possibility of planar defect interacting with Nitrogen in a neighboring lower layer that may give rise to a high spin state. (Fig 6)
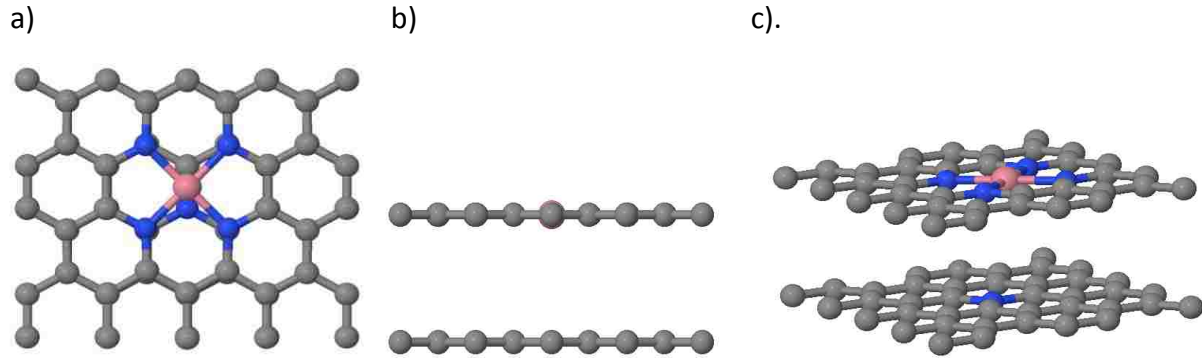
Fig 6 : Bilayer system of a TMN_4 defect with a Nitrogen substituted in the lower layer a) Top View b) Side view c) 3D view

In order to explore this option I consider bilayer graphene: the top layer will contain the $TM-N_x$ motif and the lower layer contains Nitrogen atom(s) below the TM. To explore this possibility, I did a series of computations: (Fig 7)

1. Constrain the vertical separation of the two sheets by fixing the position of the carbon atoms in the corner of the sheets.

2. Allow all remaining C, N and TM atoms to relax

3. Change relative separation of the two sheets

4. Determine maximum sheet separation which promotes out of plane motion
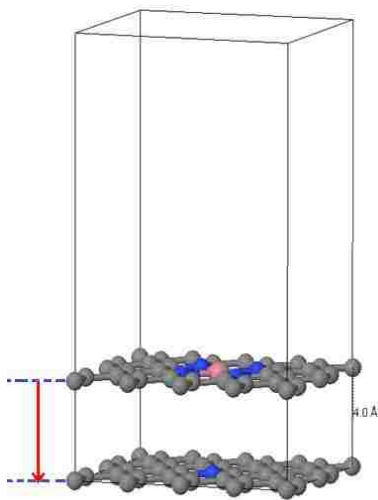
Fig 7: 3D view of a $TM-N_4$ defect in a bilayer system with sheet separation = 4 Å

Different combination of TM-N_x defects of both Fe and Co were computed (Fig 8). In the proposed bilayers, the TM-N_4 defect was placed in the top layer where the lower layer was modified with N_x atoms with x = 0, 1, 2 (where x = 0, i.e. without any Nitrogen atoms, was used as a control cell simulation) to determine the maximum sheet separation distance that promoted a high spin configuration.

a)   b)   c)
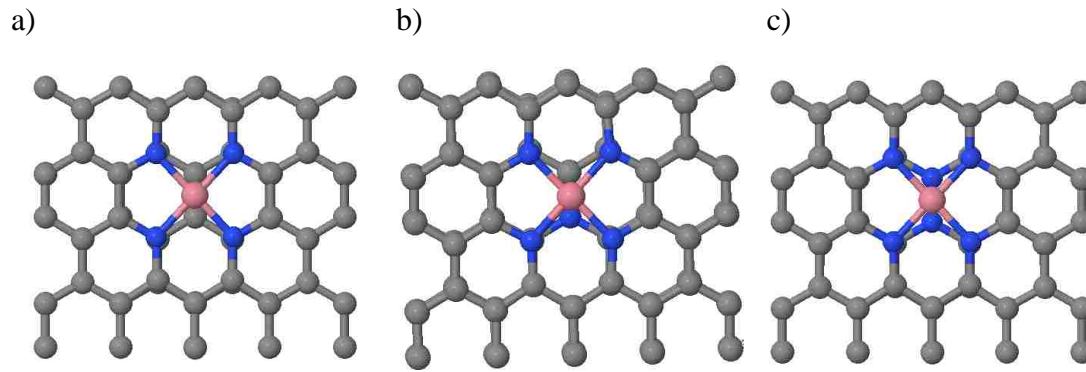
Fig 8 : TM-N_4 defects where the number of Nitrogen atoms in the lower layer are a) N = 0 b) N = 1 c) N = 2

The relative sheet separation was varied from 0.250 to 0.400 nm (2.5 to 4.0 Å). This separation encompasses the layer separation in graphite (0.335 nm) (Delhaes, P. (2001). *Graphite and Precursors*). The cut off energy was also varied from 400 eV and a softer carbon potential to ensure converged results

The magnetic moment as well as the vertical distance of both Co and Fe defects was calculated. The maximum displacement is observed at 0.350 nm (3.5 Å). This distance is also similar to layer separation in graphite, which is around 3.3 Å. The results of the vertical displacements in the bilayers are summarized below:

Vertical Displacements and Magnetic Moments of TM-N$_x$ bilayers

Vertical Displacement (Å) (CoN$_4$_C$_{32}$)			Magnetic moment (mµB)
	C_400	**C_S**	
Co	**0.19**	0.2	0.8
N (upper layer)	0.18, 0.175, 0.18, 0.175	0.20, 0.19, 0.2, 0.19	-

Table 1 : Vertical displacement of Co-N$_x$ defects (a) : N = 0 in lower layer

Vertical Displacement (Å) (CoN$_4$_C$_{31}$N)			Magnetic Moment (mµB)
	C_400	**C_S**	
Co	**0.14**	0.08	0.6
N$_4$ (upper layer)	0.135, 0.132,	0.08, 0.08, 0.08, 0.08	
N (lower layer)	0.132, 0.135 0.15	0.1	NA

Table 1(b) : N = 1 in lower layer

Vertical Displacement (Å) (CoN$_4$-C$_{30}$N$_2$)			Magnetic Moment (mµB)
	C_400	**C_S**	
Co	**0.14**	0.16	0.8
N$_4$ (upper layer)	0.14, 0.13, 0.13, 0.14	0.15, 0.14, 0.14, 0.15	NA
N$_2$ (lower layer)	0.15, 0.15	0.16, 0.16	NA

Table 1(c) : N = 2 in lower layer

From Table 1(a-c), it can be seen from these calculations that the average displacement of Cobalt out of plane is around 0.14-0.19 Å and it has an average magnetic moment of about 0.6-0.8 mµB. The bulging of the top layer does suggest the presence of am interaction between the sheets in the bilayer system. However, this interaction is insufficient to promote a high-spin state in Co.

	Vertical Displacement (Å)	Magnetic Moment (mµB)
FeN_4-C_{32}	0.44	1.9
FeN_4-$C_{31}N$	0.41	2.0
FeN_4-$C_{32}N_2$	0.45	2.0

Table 2: Vertical displacement of Fe-N_4 defect with N=0, 1, 2 in lower layer

The results from Table 2 for the Fe-N_x bilayers show that a the Fe moves out of plane by approximately 0.43 Å and adopts an intermediate spin state of 2 mµB. This implies that the interactions between the two sheets in the bilayer were not sufficient enough to induce a high spin state in either Iron and or Cobalt N_4 defects. To further investigate this phenomena, even smaller sheet separations or deviations from the N_4 defects to a different geometry, particularly TM-N_3 defects might be required.

TM-N_x single layer magnetic moments (mµB)	N_2	N_3	N_4
Co	1.0	1.0	2.3
Fe	2.5	2.0	3.11

Table 3 : Magnetic moments of single layer TM-N_x defects

Fe-N_3 defects have shown a substantial amount of deviation and a comparatively large out of plane motion of about ~1.47 Å with a magnetic moment of about ~3.1 mμB (Table 3).This is the highest moment that has been found so far. However, Fe is still not a high spin state and not the not geometry envisioned by Lefevre et al. (2012, Fig 9), which is why it is reasonable to explore other geometries and configurations which might lead to high spin states with active ORR sites.

a)   b)
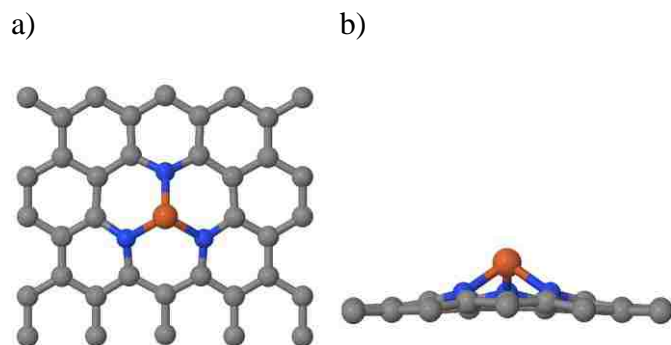
Fig 9 : Fe-N_3 defect motif a) top view b)side view

TM-N_4		TM-N_4/ N=0		TM-N_4/ N = 1		TM-N_4 / N =2	
(Nitrogen in lower layer varied from N = 0-2 from 2.5Å to 4.0Å) (Max displacement ~3.5 Å)							
Å \ μ		Vertical Displacement	Magnetic Moment	Vertical Displacement	Magnetic Moment	Vertical Displacement	Magnetic Moment
Co	1 (single)	0.19	1	0.19	1	0.14	1
Fe	2 (single)	0.44	2	0.41	2	0.45	2

Table 4 : Summary of Vertical Displacements and Magnetic Moments of TM-Nx Defects

Other Possible Defects

In the current literature on non-PGM TM-N$_x$ catalysts the ORR active site is viewed either as embedded in a Carbon matrix or as a linker between two Carbon sheets. However, our preliminary results show another possibility, namely that the TM-N$_x$ motifs provide binding between stacks of sheets (Fig 10). This insight, if corroborated shows that Nitrogen may play a dual role in these catalysts as it (i) provides bonding between otherwise weakly bound graphene sheets and stabilize the microstructure and (ii) it may provide anchoring for additional catalytic sites.

This also suggests that a secondary pyrolysis in a nitrogen rich atmosphere in the presence of a TM source may decrease corrosion of the electrocatalyst, increase durability of the catalyst and increase the number of accessible number of active sites.

a)   b)
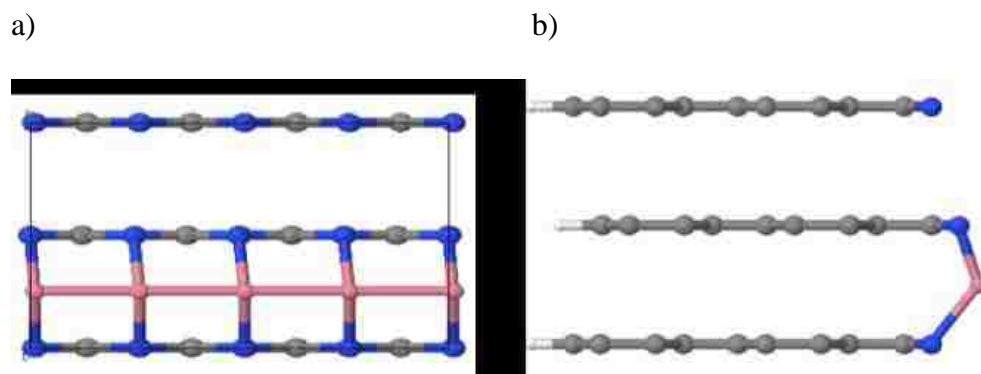
Fig 10: Inter-plane Bridges a) front view b) side view

The resulting Nitrogen edge functionalization of the Carbon sheets may form traps for TM's and hence could increase catalytic activity. Further computations are needed to reduce the TM content in the simulations. This can be accomplished by building a supercell which will allow us to separate the TM's even further
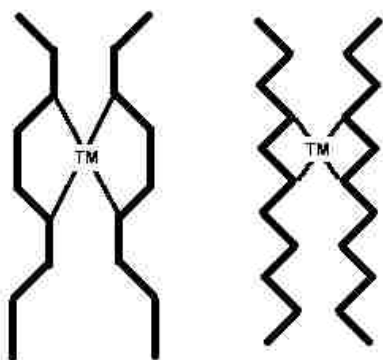
Fig 11: In-plane bridges   Fig 12: Nitrogen functionalized edges.
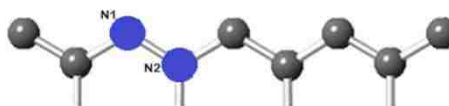
Another possible contender of TM-N_x defects are the in-plane bridges as envisioned previously (Fig 11).[12] However, these channels have a tendency to collapse due to the dangling bond interactions of edge Carbon atoms. However, functionalizing neighboring edges (Fig 12) with nitrogen could change this situation: the presence of dangling electrons repel and prevent the collapse of the channel, thus increasing the porosity of the catalyst at least at short length scales.

Chapter 3

Synergy of Computational and Experimental Methods

There is much importance on the necessity to engineer cost-effective and efficient Nitrogen containing catalysts and other novel pyrolyzed macrocycles as a material solutions and replacing platinum in polymer electrolyte membrane (PEM) fuel cells.[36] One of the main characterization techniques used for determining the chemical environment of the Nitrogen and transition metals in TM-N_x catalyst is XPS.[72] Since its introduction in 1958, X-ray photoelectron spectroscopy (XPS) has become a popular and powerful surface characterization technique for analyzing heterogeneous electrocatalysts.[36,73,74]

X-ray Photoelectron Spectroscopy (XPS)

The relatively small penetration depth of the photoelectrons makes XPS a surface sensitive probe.[75,76] This has made XPS quite essential in identifying and determining the chemical state of element, its empirical formulas, elemental composition and relative composition of the constituents in the surface region as well as the electronic states from its valence band structure.[72] In XPS, a core electron is excited into vacuum by high energy photons and the kinetic energy (E_k) of the emitted core electron is collected and measured experimentally.

The energy which is necessary to remove a core electron from an atom is called core-level binding energy (E_b). The measured core-level binding energy E_b is the energy difference between the initial, unexcited ground-state and the final, core-excited state.

This binding energy value can be determined from an energy balance: $E_k = h\nu - (E_b + \phi)$, where h is planks constant, ϕ is the work function, exactly as in the photo electric effect (Fig 13a). The X-ray photoelectron spectra (XPS) for core levels will consist of lines for each of the atomic subshells, the complexity, multiplicity, and splitting depends on the electron shell under consideration. However, quantum mechanics also shows that no splitting exists for 1s states while higher angular momenta states are split into multiplets due to electron-electron interactions in the same shell. Each element produces a characteristic set of XPS peaks at characteristic binding energy values that correspond to the electronic configuration of the elements and provides a "fingerprint" for each atomic species (Fig 13).

.

a)   b)
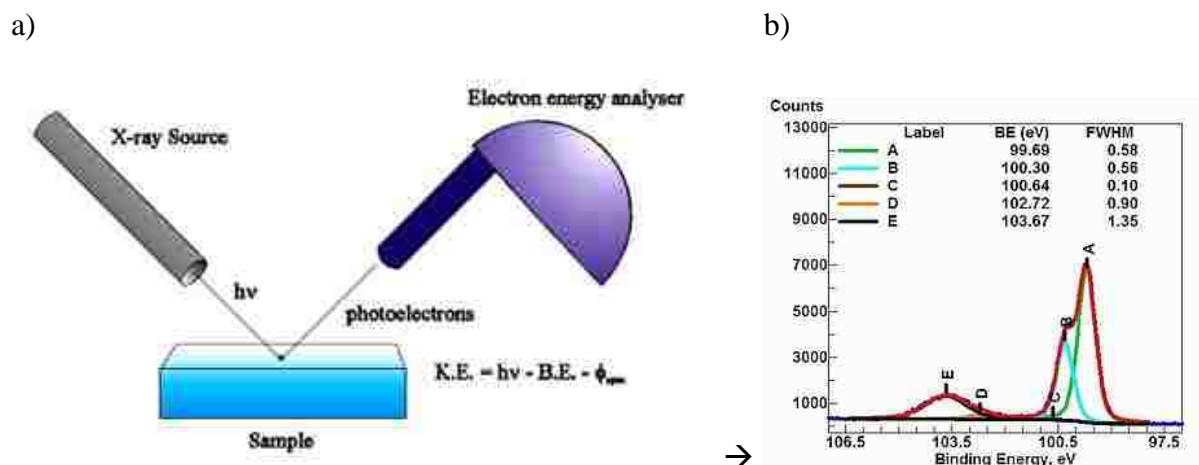
Fig 13 : X-ray Photoelectron Spectroscopy (a) setup (www.casaxps.com), b) Spectra High-resolution spectrum for Si(2p) signal.

Changes in bonding will alter shielding either through the removal or addition of electronic charge density at the nucleus. Withdrawal of valence electron charge increases the screening effect and causes an increase in E_b (oxidation) whereas addition of valence electron (reduction) charge decreases the E_b.[74]

The binding energies are typically quantified relative to the Fermi energy in periodic systems, which is in turn determined in the same experiment by exciting electrons at the Fermi edge.[77] In contrast, for molecules the reference energy is the isolated electron in vacuum and hence the electronic work function would need to be computed which may introduce additional uncertainty.

Koopman's Theorem

According to this theorem, the binding energy of an electron is simply the difference between the initial state of an atom with n electrons $E_{initial(n)}$ and the final state of the excited and ionized atom with (n-1) electrons $E_{final(n-1)}$ (ion and free photoelectron), i.e.

$$E_b = E_{final(n-1)} - E_{initial(n)}$$
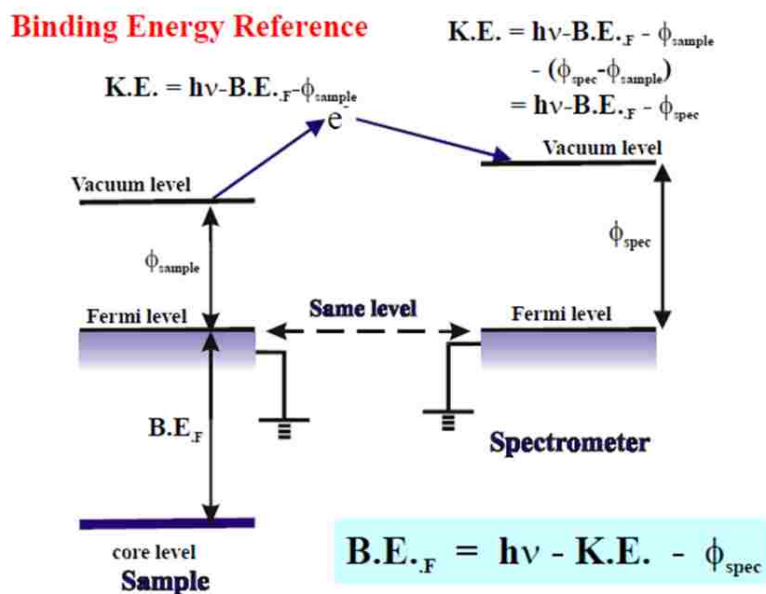
Fig 14 : Calculating Binding energies from reference states.(mmrc.caltech.edu/SS_XPS/XPS_PPT/XPS_Slides.pdf)

However, it has been recognized that binding energies are sensitive to the chemical state and local environment of the surface species because surface atoms have different chemical environments from bulk atoms.[78] These differences give rise to small shifts of binding energies which are observable by X-ray photoelectron spectroscopy. These small shifts (difference in binding energies) are known as core level shifts and they can be used to identify the structure and the binding site of the surface species (Fig 15).[74,77]

Fig 15 : High resolution N2s XPS spectrum.[79]

Limitations of XPS

Due to electronic many-body interactions, XPS spectra often have complex fine structure with several peaks of significant intensity for a given subshell. This is especially true for materials with open d or f shells.[80] The accuracy of XPS analysis depends on the signal-to-noise ratio and the peak intensity.

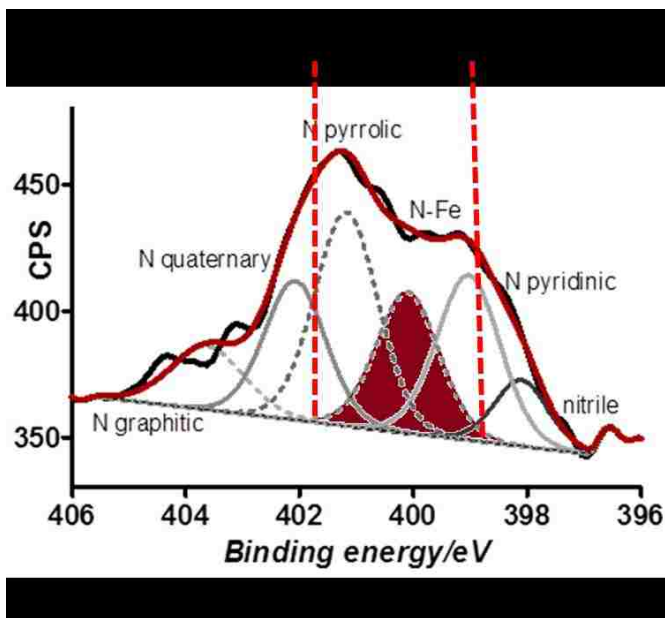Sometimes, relevant reference materials are missing and it becomes difficult to derive detailed structure/property relationships from XPS alone. Chemical shifts are found to correlate quite well with charges for gas-phase molecules and for some bimetallic systems, but this correlation has been questioned for bulk alloys and for adlayer systems.(XPS Theory, Royston Paynter,INRS-ÉMT) In practice, chemical shifts result from a complex combination of various factors, which often partially cancel. This makes it challenging to quantitatively interpret chemical shifts. Assigning peaks to the different Nitrogen coordination is challenging due to overlapping peaks that appear within a narrow energy window of FWHM ~2.5 eV. XPS which heavily relies on use of reference spectra in accurate identification of species cannot address this issue directly as no reference compounds with TM-N_2 moieties are available.

Insight into the origin of the spectral features will contribute significantly to an understanding of the electronic structure of these highly correlated materials. The binding energies as well as the core level shifts calculates using first principle calculations will be providing us with information that will be critical for identifying electro-catalytically active defect motifs.[36]

Combining XPS with DFT

It is possible to understand and appreciate the interdependencies of chemistry and morphology in carbon supported nitrogen functionalized transition metal electrocatalysts by studying the individual building blocks that are present with a variety of defects introduced in the grapheme sheets. One of the ways to identify these chemical species by means of spectroscopic methods like XPS generally involves peak deconvolution of the spectra through curve-fitting (Fig 16).

Previous work has attributed the increased ORR activity of N-containing Carbon-supported (N/C) catalysts to various N moieties (N-doped, pyrrolic, and pyridinic) as identified by XPS. [30,36] XPS observations of the electrocatalysts after pyrolysis support the presence of various TM-N_x (TM = Fe, Co, x = 2 - 4) defect moieties as possible active sites. [65] However, the location of and the specific role TM-N_x defects ORR play in ORR still remain uncertain as the N moiety responsible for the electrochemical activity of these catalysts has not been unambiguously identified and hence catalyst optimization remains challenging.
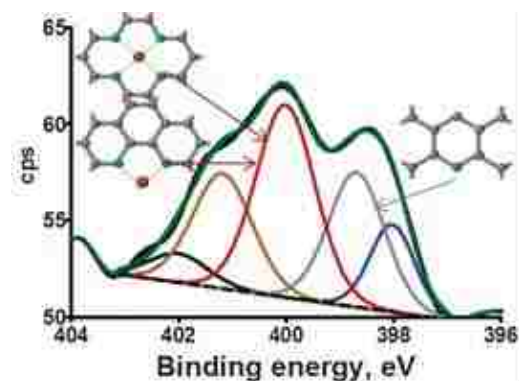

Fig 16: N1s high resolution spectra of bipyridine–Fe catalysts[36]

In practice, chemical shifts result from a complex combination of various factors, which often partially cancel. This makes it challenging to quantitatively interpret chemical shifts.[61] Also, the correlation between features in the XPS spectra and particular defect geometries and chemistries remains challenging and generally relies on the availability of suitable reference materials. In the absence of these reference materials the interpretation of Nitrogen speciation based on N1s core level shifts is more tentative. Therefore it is required to provide independent estimates of core level shifts for assumed defects. On one hand, the presence of an XPS peak with certain energy is taken as a fingerprint that a particular atomic or molecular species is contained in the material. At a more sophisticated level, the core level binding energies are used to obtain in-formation about the chemical interactions and chemical bonding in which the core ionized atom is involved.[81] First-principles computations can provide this missing link by predicting core level shifts for candidate chemistries and geometries of the catalytic sites. Interpretation of observed XPS spectra can be supported by theoretical calculation as calculated chemical shifts are likely to become an important tool in analyzing surface species and surface structures.[36]

In the following sections, a comprehensive review of different mechanisms which contribute to the chemical shifts of core-level binding energies is made. I focus on mechanisms which can be used to relate the core level shifts to features of chemical bonding and chemical interactions in the studied system. When all of the relevant mechanisms are taken into account in the analysis of the shifts in binding energies, these shifts do provide valuable information about the chemical bonding and electronic structure of the materials being studied.

Chapter 4

Using DFT to Calculate Binding Energies and Core Level Shifts

Density functional theory (DFT) has become an important modeling based analytical tool in studying heterogeneous catalytic reactions.[1,25,82] Above all, advances made in DFT computations now means that it is now possible to calculate the relative stability of various possible reaction intermediates and the activation barriers of surface reactions routinely with high accuracy.[74] In addition, calculating chemical shifts can help identify the structure and the adsorption site of surface species and catalyst promoters.[74,83] Information obtained from DFT calculations can be used as input for determining core level shifts which in turn can be used to interpret the XPS spectra.[61]

Initial and Final State Approximations

In density functional theory, there are several schemes used in calculating the binding energy of core electrons and their chemical shifts, where relaxation is either taken into account or disregarded. Core level shifts can be and generally will be affected by electronic relaxation in the computations.[84] Chemical shifts in the core level binding energies have been interpreted as initial-state effects originating from changes in the electrostatic interactions between the core electrons and the valence electrons and the final-state effects arising from charge rearrangement and relaxation occurring in response to the core hole. Core electron binding energies can be calculated either in the initial state approximation or the final state approximation.[81,85]

In the initial state approximation the core electron is removed but no change of the potential (e.g., by relaxing other electrons) is allowed. Electronic screening is therefore entirely neglected. The core electron binding energy in the initial state approximation can be calculated from the Kohn-Sham eigenvalues of the core state of interest.[81,84] In the final state approximation, a single core electron is excited from the core to the valence shell, and the electrons are allowed to relax after the core electron has been removed, so that the acquired localized hole is screened. Since the valence electrons screen the localized core hole rapidly in metals (sudden approximation), the core electron binding energy shifts between the bulk and the surface are expected to agree well with experiment in the final state approximation.[81,84,86]

The preliminary results were computed without taking relaxation into account. The significance of this additional parameter relies on the knowledge of the lifetimes of the excited states which at present remain unknown. We will discuss several computational protocols to compute core level shifts from first-principle simulations and the effect of relaxations in the final state.

Our binding energies were calculated in the final state approximation as the energy difference between two separate calculations where[74,81]:

(i) the first calculation is a typical DFT calculation in which the no. of core electrons correspond to the unexcited ground state $E_{initial(n)}$

(ii) and the second calculation is where an electron is removed from the core of the particular ionized atom (i.e. a single electron excitation) and added to its valence band $E_{final(n-1)}$.

The energy difference is a measure for the experimentally determined core-level binding energy:

$$\mathbf{E_b = E_{final(n-1)} - E_{initial(n)}}$$

DFT Calculations: Computational Approach

In the present study, first-principles calculations are performed on a set of candidate structures to simulate experimental measurements by studying the chemistry and geometry of ORR active TM–N_x/C (x = 2- 4) from the binding energies and core level shifts of different motifs and demonstrate that C1s and N1s and Fe2p/Co2p chemical shifts can be calculated accurately using DFT.[1]

Computation Methods

All DFT computations were carried out using VASP at the GGA level using a periodic 3-D plane wave simulation cell.[52,58-60] The original Carbon support was modeled as a 2-D Carbon sheet (grapheme like structure) that contained 32 atoms with Nitrogen and transition metal atoms (Fe, Co) introduced as substitution where DFT calculations are being carried out.

All-electron like PAW potentials are used to describe the interactions between valence electrons and nuclei.[62] Spurious interactions between the modeled sheet and its periodic images perpendicular to the sheet were eliminated by introducing a 14 Å thick vacuum layer and by applying a dipole correction to the total energy. For geometry optimization, a plane wave energy cutoff of E_{cut} = 800 eV was used throughout the computations and a 8x8x1 Monkhorst–Pack grid to obtain converged results.[64] The core-level binding energies were calculated using single electronic excitations and in the final state approximation as implemented in VASP.

Challenges with DFT

Potentials

There are quite a few challenges associated with DFT as the calculations are computationally demanding and not very straightforward. While doing structural relaxations and initial state approximations, it's usually the valence band electrons which are taken into account. However, the core electrons are not modeled in this approach and usually the information regarding the core electrons is discarded during the generation process of the pseudopotential. However, the VASP library of potential retains this information as the PAW potentials happen to retain knowledge of these core electrons and hence provide access to core electron properties.
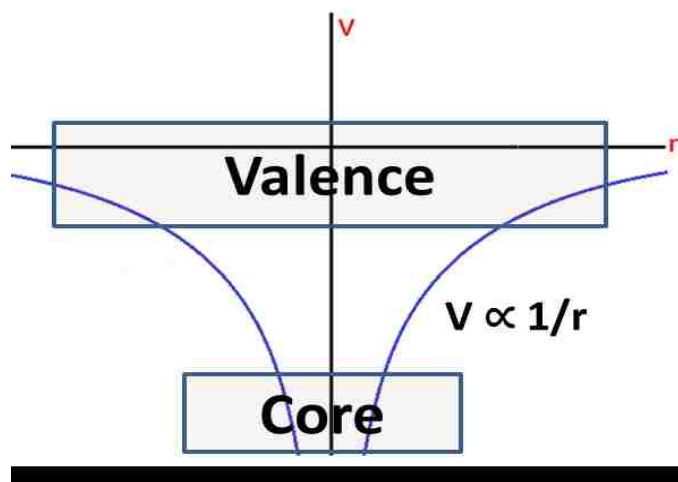

Fig 17 : Potentials near the nucleus

During a standard computation this part (core electrons) of the potential is simply ignored. (Fig 17) It should be emphasized that this methodology cannot be expected to reproduce absolute values for the core level binding energies, due to the steep Coulomb potential near the nucleus where small errors in wave functions get amplified.

The proposed solution to this challenge is to compare binding energies in the system of interest to a reference system that is available both experimentally and in theory so that we focus on the binding energy *shifts* (difference in binding energies) rather than the exact binding energies themselves. Relative energies can be calculated and interpreted more easily than the absolute binding energies with an accuracy of ~ 5.0 -20 m eV as shown in our calculation.

K Points :

Another important factor that needs to be taken into consideration are the K point grids we use for doing our calculations. In electronic structure theory, the complex wave functions are presented in the form of periodic Fourier transforms : $F(x) = \sum C_i\, e^{\,iK\,i\,x}$ and the 3D K points grids are the maximum no. of divisions in the x y and z directions, $K_i = 2\pi/K_{imax}$ which need to be specified by the user (Fig 18)
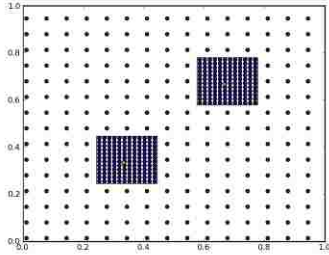

Fig 18 : 2D Brillouin zone of a surface with cubic symmetry with a 8x8 Monkhorst-Pack grid (http://th.fhi-berlin.mpg.de)

However, these K point grids also depend on the computational resources available to the user and the size of the system under study. In theory, the denser the K point grid, the more accuracy that can be achieved, but that will require additional computational power. We therefore will evaluate multiple K points to optimize the least dense grid needed to obtain a converged results

Analysis

Core electron binding energies will be calculated for the N1s, Fe2p and Co2p core state in the final state approximation. Among the numerous schemes developed to calculate core level binding energies using DFT,[87] the final-state approximation is most accurate one where a single core electron is excited by generating the corresponding core excited ionic PAW potential in the course of the *abinitio* calculations. In this assumption, the core hole remains entirely localized at the excited atom, which is usually a reasonable approximation and is expected to agree well with experiment.[81] Once the computations were complete, the structures were visualized using the different modeling softwares available (Ex, Jmol, Crystal Maker) to obtain intermediate results. Post processing of the output from the DFT calculations acquired was then analyzed to determine evolution of the transition metals magnetic moment as well as the binding energies and core level shifts of the defect motifs. The outputs we use for our analyses are as follows:

Fermi Level Energy (E_{fermi}) : hypothetical level of potential energy for an electron inside a crystalline solid

Eigen Energy (Kohn-Sham energy, (E_{KS})) : corresponds to a quantum state with a specific energy and this is obtained using the Kohn-Sham equations [52,53,88]

We then use E_{fermi} and E_{KS} to calculate binding energies of the N1s, Fe2p and Co2p orbitals as

Binding Energy = Kohn-Sham Energy (N1s, Fe2p, Co2p) – Fermi Level Energy

$E_b = -(E_{KS} - E_{fermi})$

Core level shift $CLS = B.E_{motif} - B.E_{reference}$

Sign convention for CLS

CLS > 0 signifies: defect structure has a less negative energy eigenvalue than the reference structure. == Binding energy of the defective structure decreases relative to the binding energy of the reference state. This gives rise to a downward (negative) shift.

CLS < 0 signifies: defect structure has a more negative energy eigenvalue than the reference structure. == Binding energy of the defective structure increases relative to the binding energy of the reference state This gives rise to an upward (positive) shift.
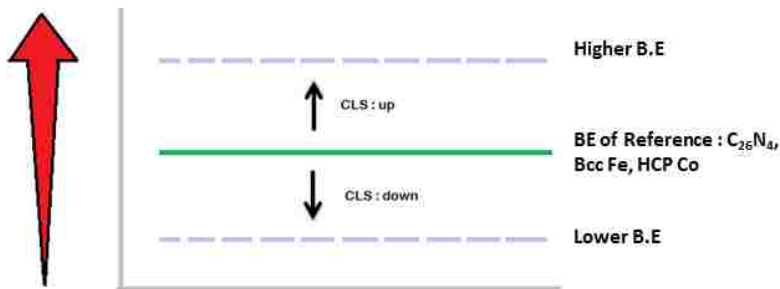

Fig 19 : Relative binding energy shifts - up and down.

Throughout this work we follow the convention that higher (more positive) formation energy (binding energy) means that the presence of a defect in the equilibrium (weaker interaction) is less likely.[1]

Chapter 5

Results and Discussion

Reference structures:

The reference structures used to calculate the binding energies and core level shifts should be chosen in such a way that they are accessible both computationally and experimentally. The reference structures which we have selected to do our core level shift calculations are as follows:

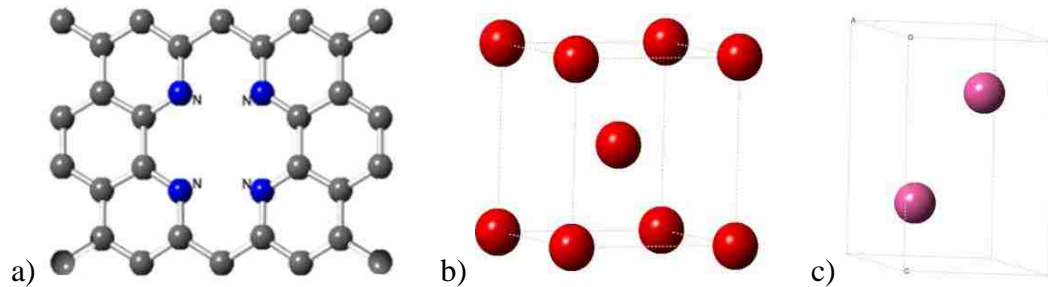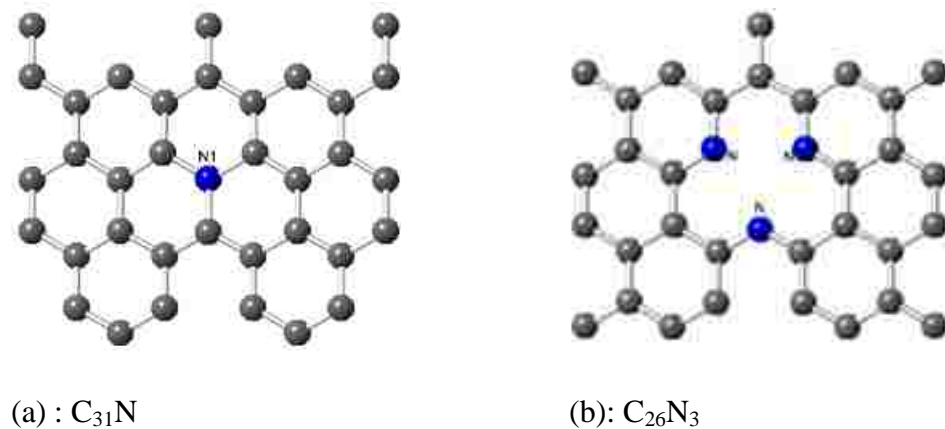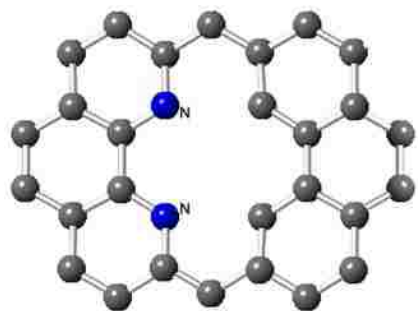N1s : $C_{26}N_4$, Fe2p : BCC-Fe, Co2p : HCP- Co
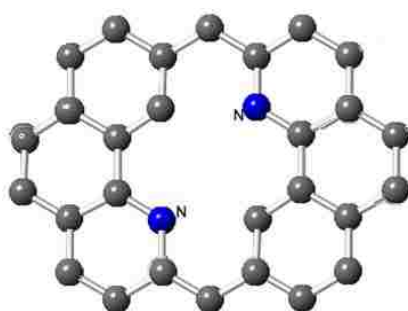
Fig 20 : Reference structures

The Defects

Non-Metal Family : In-plane/graphitic CN_x defects embedded in graphene modeled as Grey: C, blue: N

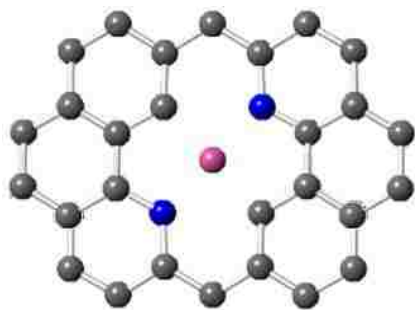(a) : $C_{31}N$ (b): $C_{26}N_3$
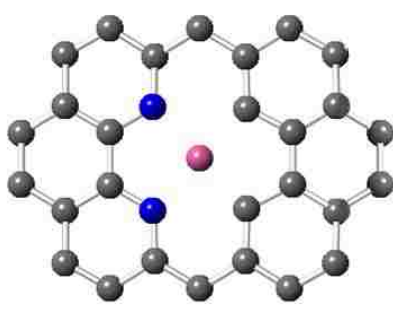
(c) : $C_{30}N_2$(C1)　　　　　　　　(d) : $C_{30}N_2$(C2)
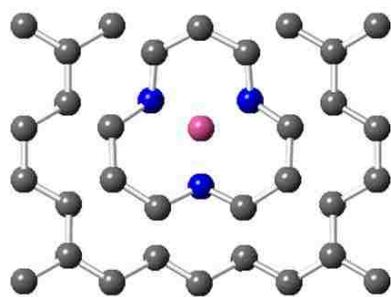
Figure 21(a-d) : Non-Metal Family Defect motifs.

Metal Family : In-plane/graphitic TM–N_x defects embedded in graphene modeled as a Carbon support for a transition metal based non-PGM catalyst. (Color code : Grey: C, blue: N and Magenta : Fe/Co atoms)
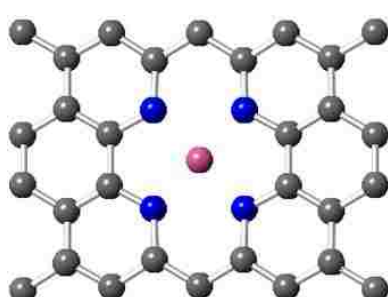

a) TMN_2C_{28}(C1)　　　　　　　　b) TMN_2C_{28}(C2)

c) TMN_3C_{28}　　　　　　　　d) TMN_4C_{26}

Figure 22 (a-d) : TM-N_x Metal Family defect motifs

39

VASP 4.6.34 vs. VASP 5.2

All binding energies were calculated using final state approximation where the structures were allowed to relax after excitation using two different versions of VASP (VASP 4.6.34 and VASP 5.2/Stampede) This was done to ensure the results we obtain are consistent in terms of accuracy and calculated in the same platform, thereby eliminating all possible computational biases. Our results that there was a difference of 1eV in the absolute core level binding energies of the defects. However, the core level shifts were consistent with the core level shifts we calculated using VASP 4.6. We can now assume that out calculations are bias free and are fairly certain that the core level shifts do not depend on the version of software we use as long as all necessary computations are performed with the same software release.

Convergence Test

Multiple K-points grids were evaluated to optimize the least dense grid with computation power and this was intrinsically done to show that we do obtain converged results (Table 5). The defect used for this convergence test was the $C_{26}N_4$ defect used for single-electron excitation binding energy calculations for a planewave energy cut-off of 800 eV. The effect of changing K-point grid is shown in Fig 23. It can be observed that the oscillations are pretty well behaved and it is the 881 k point grid with the lowest converged Eigen energy. Using this grid we also achieve an accuracy of around 5 meV, which is much higher than that of XPS. We therefore, have chosen the 8x8x1 K Point grid to be the reasonable compromise between accuracy and computational power.

K Point Grid	Eigen (Kohn-Sham) energy	Fermi Energy	Binding Energy
4x4x1	-436.8172	-2.3743	-434.4429
6x6x1	-436.8485	-2.3438	-434.5047
8x8x1	-436.8495	-2.3585	-434.491
10x10x1	-436.8459	-2.3561	-434.4898
12x12x1	-436.8473	-2.3537	-434.4936

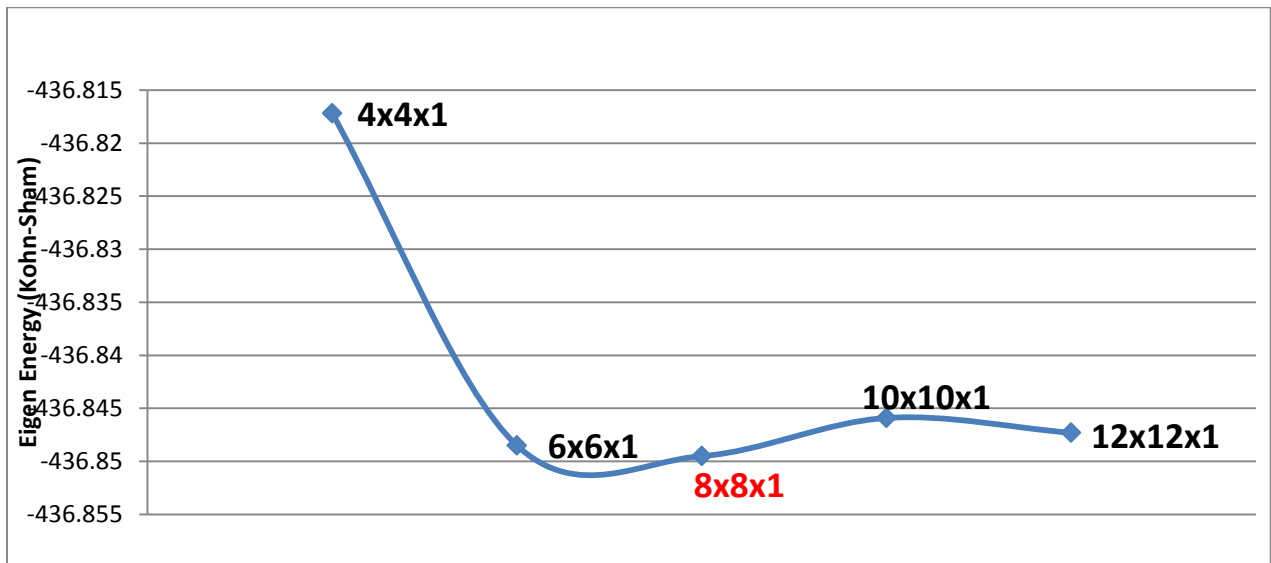Table 5: Eigen, Fermi and Binding Energies of $C_{26}N_4$ N1s orbitals

Fig 23 : K points convergence test

The 8x8x1 K-point grid was chosen to be optimized reasonable compromise between computational resource requirements and precision. As Fig. 23 shows starting from a 6x6x1 k-point grid changes in the core level binding energies are less than 5 meV, significantly lower than the precision obtained in XPS experiments. It is important to note that the changing vacuum height from 14 A to 18 A did not change the results.

Multi vs. Single Electron Excitation

The incoming flux of the x-ray beam might have an impact on the excitation process of the photoelectron due to the symmetry and geometry of the Carbon and Nitrogen atoms. In a single electron excitation, the core electron is excited into vacuum by high energy photons. (Fig 24a) In a multi electron excitation, the core electron is removed by photo absorption along with an outer shell electron (Fig 24b). Perhaps a high efficiency of the incoming x-ray beams might induce a high rate of photoelectron emission. X-ray photoabsorption spectra are usually construed in the context of the one-electron approximation. Conversely, the existence of the multielectron excitation process, where the removal of a core electron by photo-absorption causes excitation or ionization of additional electrons from shallower orbitals of the same atom, has been known in XAS for a long time. However, according XPS and DFT in literature[61,81] photoabsorption process is usually construed in the context of the one-electron approximation.[61] To evaluate the sensitivity of core level shifts to electronic excitation, I evaluate both single as well as multi electron excitation.
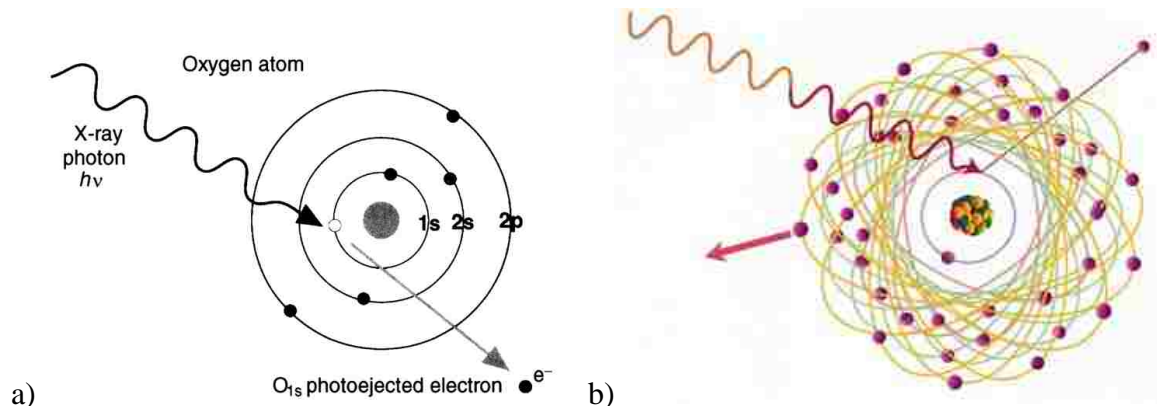

a)   b)

Fig 24 : Electronic Excitations: (a) Single, (Photoemission) b) Multi (http://www.chem.uniroma1.it/dangelo/research.html)

Core Level Shifts (Single Electronic Excitations)

The reference structure to calculate the binding energies of N1s and Fe2p binding energies used were the pyridinic type $C_{26}N_4$ defect and BCC iron respectively. The cut off potential was 800 eV and all binding energies were calculated using the final state approximation.

N1s shifts for CN$_x$ Non-Metal Family

Defect	DFT (eV)	Shift	XPS (eV)
$C_{26}N_3$	0.3	down	NA
$C_{28}N_2$(C1)	0.3	up	NA
$C_{28}N_2$(C2)	0.1	up	
$C_{31}N$	3.3	up	3.0 - 4.0

Table 6 : N1s core level shifts (single e-) for non-metal family

N1s Shifts for TMN$_x$ Metal Family

Defect	Fe (DFT)		Co (DFT)	
	N1s (CLS) eV	Shift	N1s (CLS) eV	Shift
TMN_2-C_{28} (C2)	0.9	up	0.8	up
TMN_2-C_{28} (C1)	1.1	up	1.1	up
TMN_3-C_{26}	1.5	up	1.5	up
TMN_4-C_{26}	1.5	up	1.3	up

Table 7 : N1s core level shifts for metallic family

TM-N$_x$ Core level shifts : N1s Single vs. Multi Electronic Excitations

N1s CLS (eV)	Single	Multi
Co-N$_2$(C1)	0.8	0.9
Co-N$_2$(C2)	1.1	0.8
Co-N$_3$	1.5	1.1
Co-N$_4$	1.3	1.4

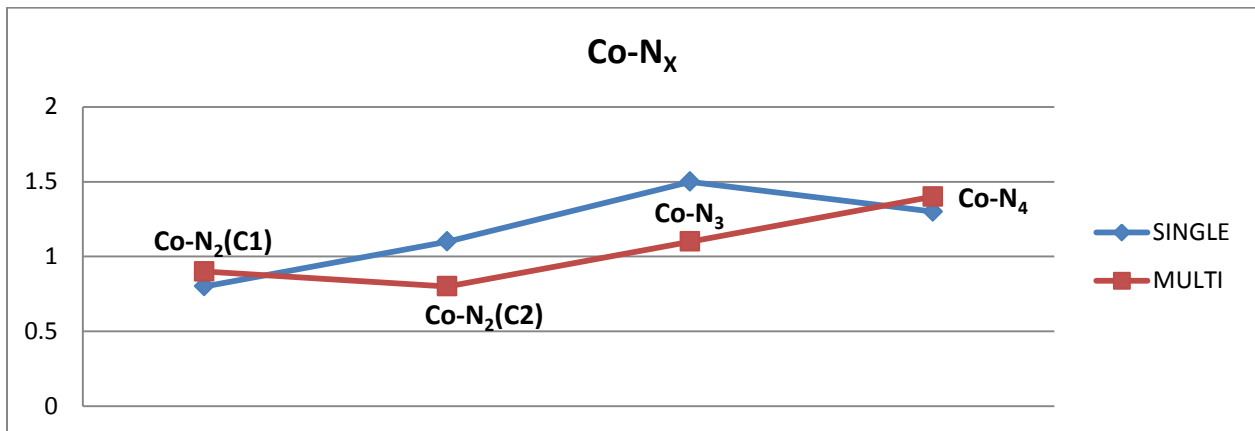| N1s CLS (eV)	Single	Multi
Fe-N$_2$(C1)	1.1	1.0
Fe-N$_2$(C2)	0.9	1.1
Fe-N$_3$	1.5	1.0
Fe-N$_4$	1.5	1.5

Table 8 : TM-N$_x$ CLS, multi vs. single

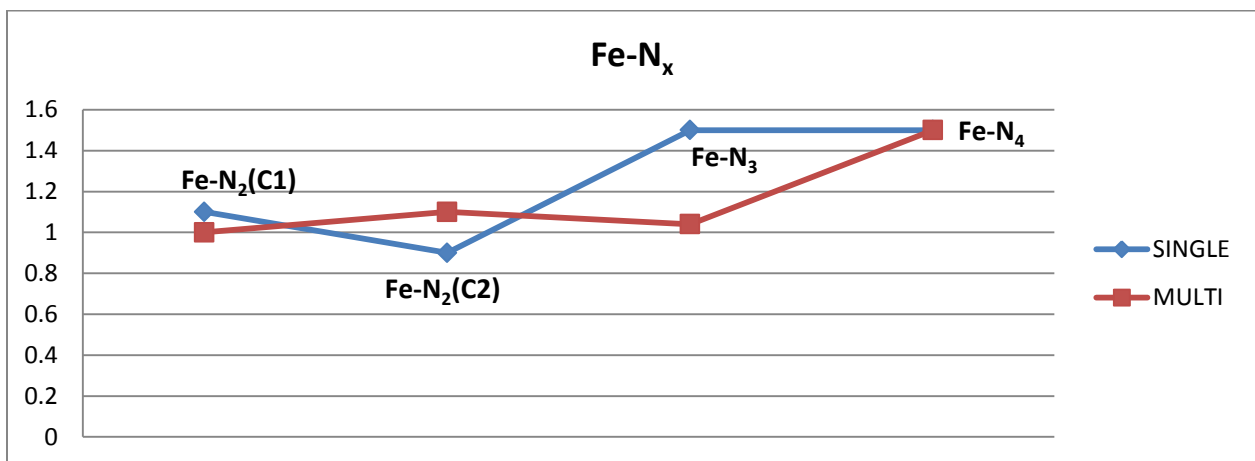Fig 25 : Trend in N1s core level shifts for Co-Nx

Fig 26 : Trend in N1s core level shifts for Fe-Nx

Fe-N$_x$ Core level shifts : Fe2p Single vs. Multi Electronic Excitations

Fe2p CLS (eV)	Single	Multi
Fe-N$_2$(C1)	0.3	0.4
Fe-N$_2$(C2)	0.3	0.4
Fe-N$_3$	1	1.1
Fe-N$_4$	0.3	0.4

Table 9 : Fe2p Core level shifts of Fe-Nx defects
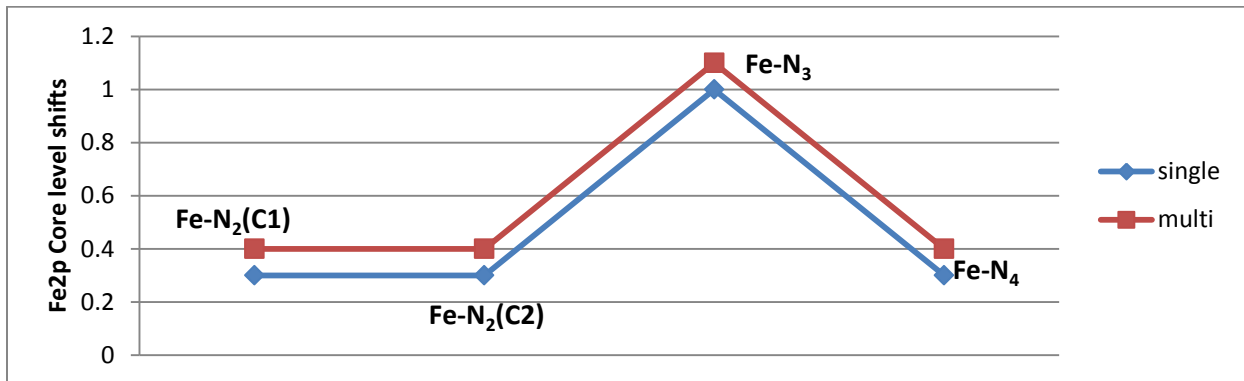

Fig 27 : Trend in Fe2p core level shifts for Fe-Nx

The results from Table 8-9 and Fig 25-27 suggest there is a difference in about 0.5 eV in core level shifts when the core electrons are as single and multi electronic excitations, respectively. Interestingly, this could be of interest which could come into play for the interpretation of high intensity X-ray sources that may promote multi electron excitations. However, we follow previous work[61] and focus on single electron excitation which has been suggested as the dominant type of excitation. Also, our final state single electron excitations have been shown to have a good agreement with experimental studies, and we will use this methodology for the rest of our calculations.[36]

Experimental Data

Reference structure available in experiment: N-Pyridinic (399.8 eV)[36]
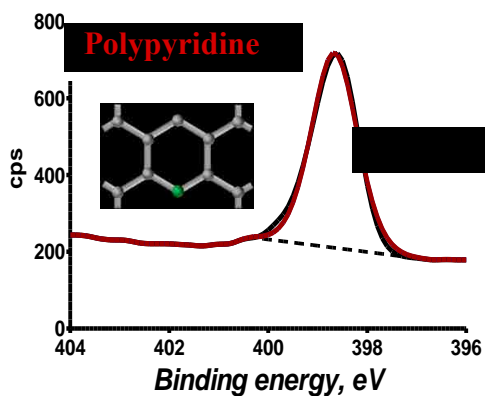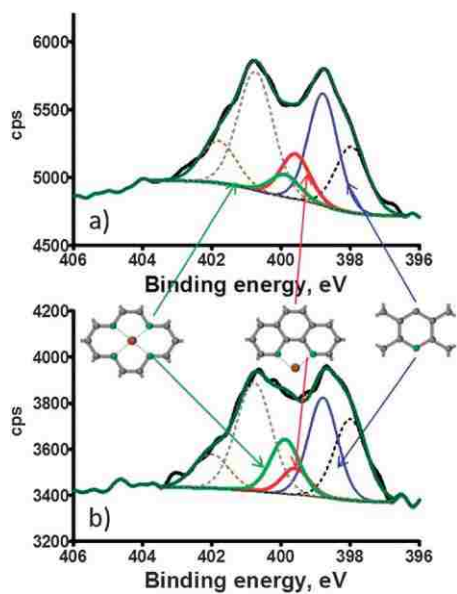

Fig 28 : Polypyridine : N-Pyridinic

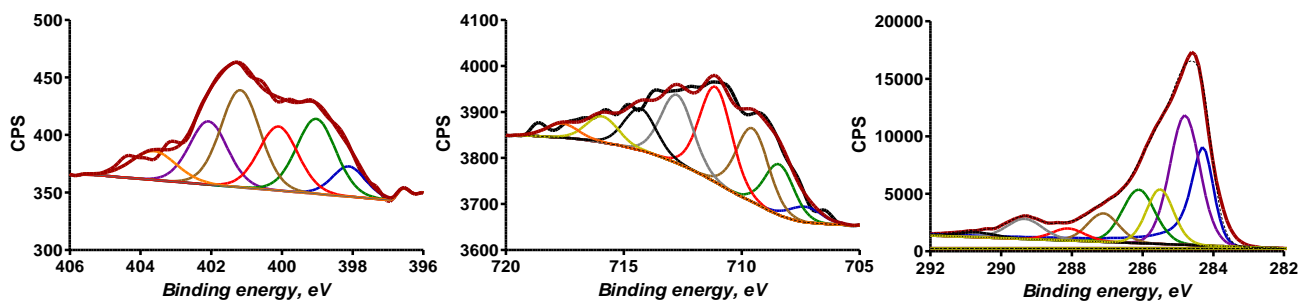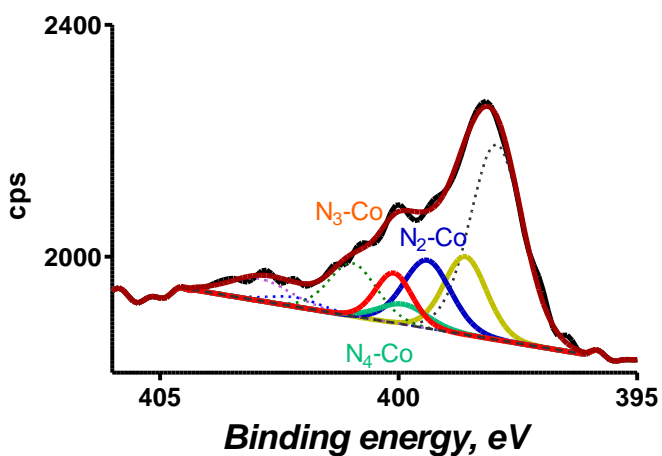Fig 29 : XPS Binding energies of Co-Nx moieties.

Fig 230 : Experimental Data with no input of DFT(Kateryena Artyushkova)

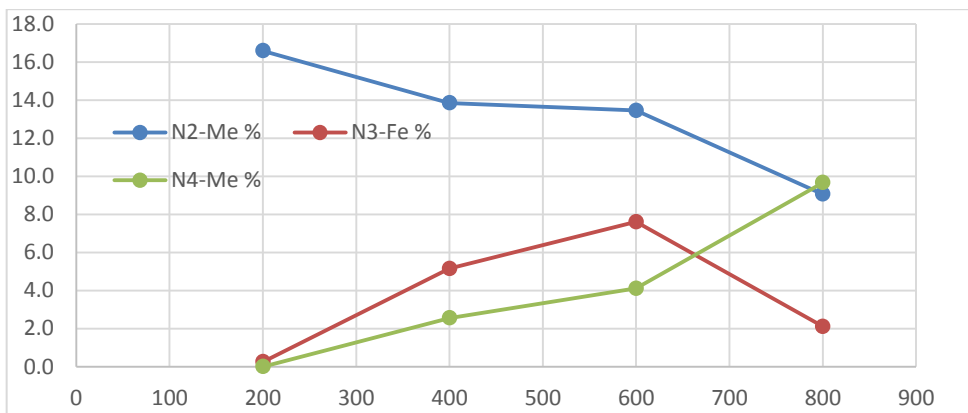## Co-N$_x$ Core Level Shifts : DFT vs. Experiment

Cobalt Defects	N1s CLS (DFT) eV	N1s CLS (Experiment) eV
CoN$_2$-C$_{28}$ (C2)	0.8	0.9 − 1.1[36]
CoN$_2$-C$_{28}$ (C1)	1.0 − 1.1	-
CoN$_3$-C$_{26}$	1.5	N/A
CoN$_4$-C$_{26}$	1.3	1.1[36]

Table 10 : N1s core level shifts of Co-N$_x$ defects

a)

b)

Figure 31 : N 1s fit for Co-TMPP using a) DFT input(top) b) stability of Co-Nx defects as function of pyrolysis T

Fe-N_x N1s and Fe2p Core level shifts

Defect	Fe2p		N1s	
Iron	DFT	Experiment	DFT	Experiment
FeN$_2$-C$_{28}$ (C1)	0.3	N/A	1.1	N/A
FeN$_2$-C$_{28}$ (C2)	0.3	N/A	0.9	N/A
FeN$_3$-C$_{26}$	1	N/A	*1.5*	N/A
FeN$_4$-C$_{26}$	0.3	N/A	*1.5*	1.1

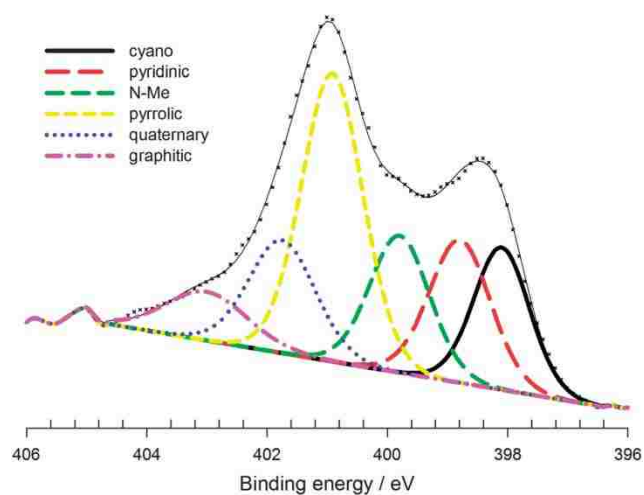Table 11 : N1s and Fe2p core level shifts of Fe-N_x defects

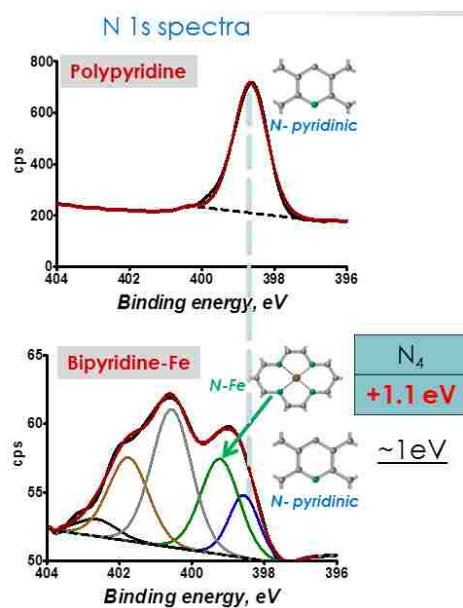Fig 32 : High resolution N 1s spectra of Fe–AAPyr (Artyushkova, K, J. Mater. Chem. A, 2013, xx, 1–8)
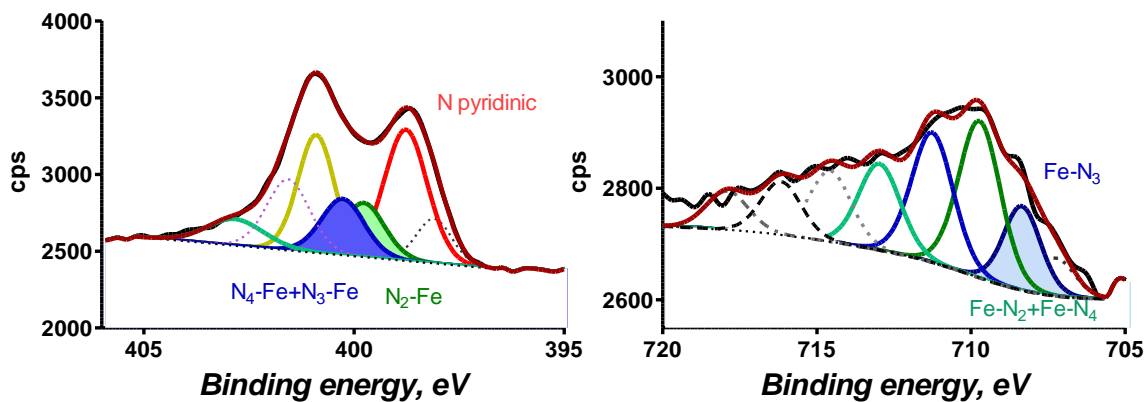

Fig 33 : XPS Binding energies of Fe-Nx moieties.

Fig 34 : N1s fit for Fe-N_x catalysts using DFT input

Stability Data:
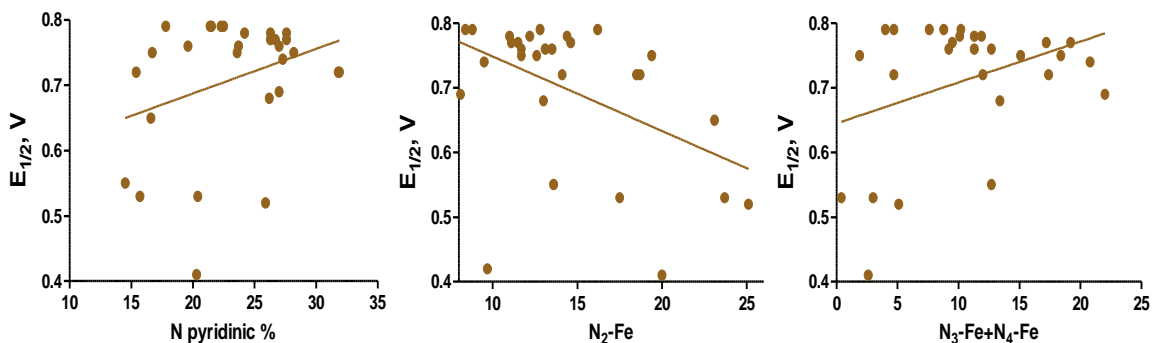
Fig 35 : Correlations between N and activity using DFT input

TM-N_x	N_2		N_3		N_4	
	Formation Energy(eV)	Critical Voltage(V)	Formation Energy (eV)		Formation Energy (eV)	Critical Voltage(V)
Co	-0.9	0.45	-3.6	-	-1.4	1.78
Fe	-0.5	0.27	-3.1	-	-1	1.55

Table 12 : Thermodynamics of TM-N_x defects

CHAPTER 6

INTERPRETATION OF CORE LEVEL SHIFTS

Nonmetal Family

C$_{31}$N : Experimental Validation

Fig 36 : C$_{31}$N defect motif. (Gray : Carbon, Blue : Nitrogen)

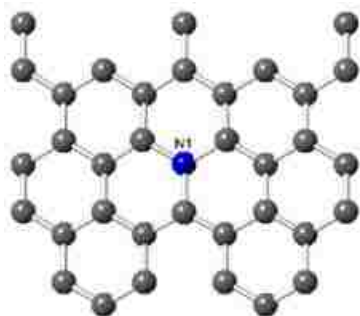Our calculations show that the C$_{31}$N defect moiety is predicted to have a very large and positive core level shift of 3.3 eV (Table 6). This is also in agreement with experimental data as it falls within in the range of the XPS core level shift of 3.3-4.0 eV (Fig 37).[79] Several groups in the past have supported the idea that metal free nitrogen doped carbon may be ORR active.[89,90] A few lines of evidence suggest this may not be the case. The low intensity of the C$_{31}$N peak in the N1s XPS spectra of nitrogen functionalized Iron catalysts suggest that it is of low abundance compared to the Fe-N$_x$ defects and might not contribute much to ORR activity. Previous studies have shown that nitrogen doped carbon obtained from oxidized Carbon that is heat-treated in ammonia at a very high temperate (~900 C) showed a 0.510 V vs. SHE onset potential toward oxygen reduction.[89] Observations made during RRDE experiments suggest that the reduction reactions taking place on C$_{31}$N motifs are mainly by the two-electron process which produces hydrogen peroxide.
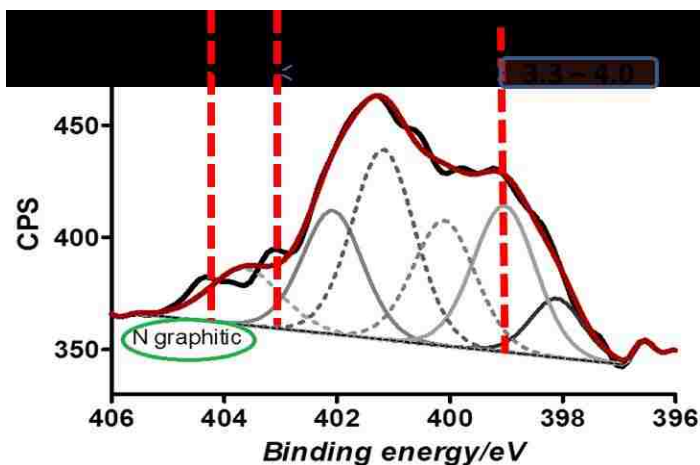
Fig 37 : XPS binding energy shifts of nitrogen doped graphite $(C_{31}N)$[79]

$C_{31}N$	
Formation Energy (eV)	0.9
Magnetic Moment (mµB)	0

Table 13: Magnetism and Energetics of N doped graphene

However, while nitrogen doped carbon may be present in the as-prepared catalyst it is unlikely that it is present under operating conditions. It has an endothermic formation energy of +0.9 eV, and hence this defect is predicted to be kinetically stabilized (Table 13). It is also important to point out that it remains unclear if the transition metals while present in the precursors needed to produce these $C_{31}N$ catalyst defects can be completely removed during acid wash or if small remaining amounts of transition metals may affect the overall catalytic activity. The initial activity may well be due to all the defects present in the catalyst but over time $C_{31}N$ might corrodes away leaving only TM-N_2 and TM-N_4/N_3 defects behind.

Carbon-N_2/N_3 Defects : DFT Predictions
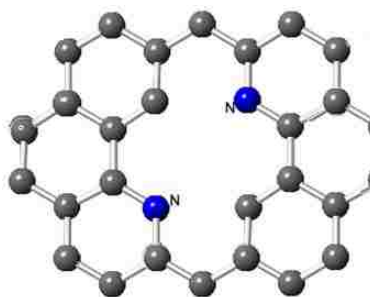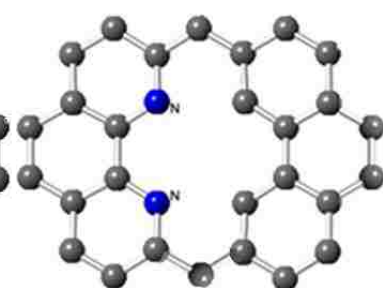
a) $C_{28}N_2$(C1)   b) $C_{28}N_2$(C2)   c) $C_{26}N_3$
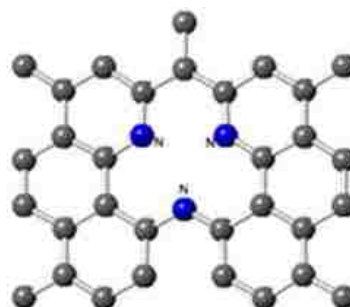
Figure 38 : Carbon-N_2/N_3 Defects

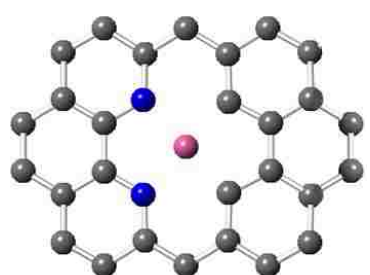The core level shifts of carbon N_2 and N_3 (non-metal) defects range from 0.1-0.3 eV (Table 6). The calculated core level shifts obtained suggest that they might not be as ORR active as their metal counter parts and are predicted to have average abundance and stability.

Transition Metal Family

TM-N_2 defects:

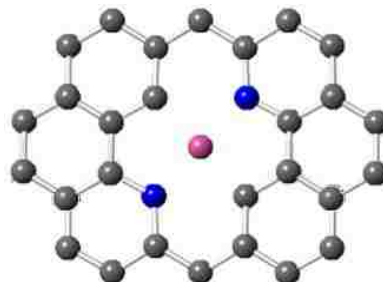a) TMN_2-C_{28} (C1)   b) TMN_2-C_{28} (C2)

Fig 39: TM-N_2 defect motifs.

Our calculations (Table 7) have shown that the N1s core level shifts of Fe-N$_2$ defect motifs range from 0.9-1.1 eV and these findings are consistent with Co-N$_2$ core level shifts which are also predicted to be about 0.8-1.1 eV. Moreover, these results agree well with experimental values of 0.9-1.1 eV for Co-N$_2$ defects[36] (Fig 40) and this has helped us establish a connection between experiment and theory. Based on the analysis above, the similarities in TM-N$_2$ shifts clearly indicate that the core level shifts depend weakly on the detailed arrangements (C1 and C2 configuration) of the Nitrogen atoms, as expected.
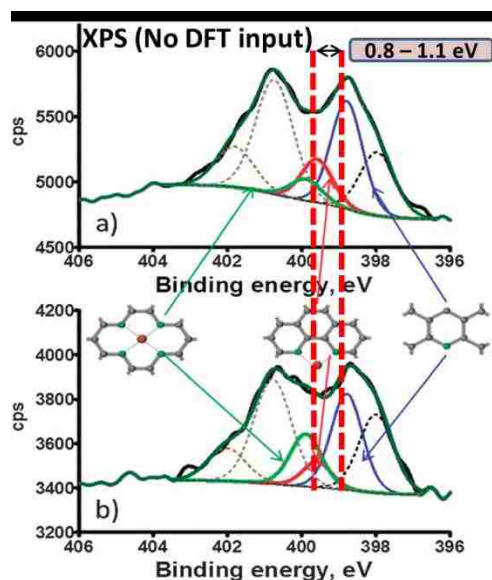
Fig 40 : N1s XPS Spectra of Co-N$_x$ defects[36]

TM-N$_2$ defects are also predicted to have a fairly large abundance as indicated by the magnitude of their corresponding peaks in XPS, and their abundance might increase with increasing pyrolysis temperature during synthesis. However, previous calculations have shown that the formation energy of Co-N$_2$ changes sign at the critical volate of 0.45 V (Table 12), indicating that this defect is likely to be unstable at potentials that are relevant for fuel cell and or even higher potentials.[1]

TM-N$_3$ and TM-N$_4$ Defects
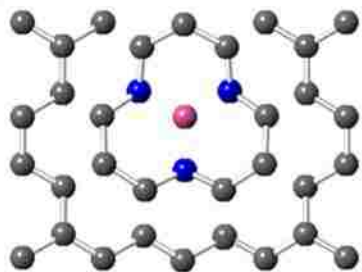
a) **TMN$_3$-C$_{26}$**   b) **TMN$_4$-C$_{26}$**

Fig 41 : TM-N$_4$ and TM-N$_3$ defect motifs

The DFT predicted N1s core level shift of Fe-N$_3$ and Co-N$_3$ defects both have a similar shift of 1.5 eV and we anticipate these defects to be the energetically favorable in terms of activity and stability as per their abundance in the XPS spectra and formation energies. (Table 11-12) The ground state of Fe-N$_3$ is predicted to be ferromagnetic with a magnetic moment of about 3.1 mμB. The DFT predicted N1s core lev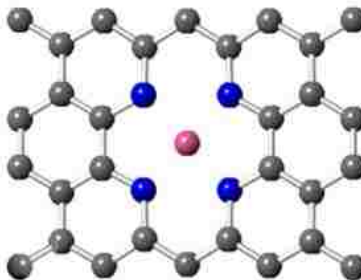el shift of Fe-N$_4$ and Co-N$_4$ are of 1.5 eV and 1.3 eV, respectively. The core level shifts of Fe-N$_4$ are in fair agreement with experimental XPS core level shift of ~1.1 eV as it is well within the Fe-N$_x$ peak in the N1s XPS spectra (see Fig 25) When compared to experimental data, the order and direction of the core level shifts remain the same. However, the shifts for Co-N$_4$ increased slightly in the order: Co-N$_4$ > Co-N$_2$. This could imply that the Co-N$_4$ defect is more stable than Co-N$_2$ defect. Overall we find that the core level shifts of Co-N$_x$ defects increase in the order : N$_3$ > N$_4$ > N$_2$. The prediction of a higher upward shift for Co-N$_4$ as compared to Co-N$_2$ is consistent with experimental observation.[36] Furthermore, the computations predict that the Co-N$_3$ defect shows a larger and distinct shift, thus should be identifiable in experimental N1s spectra.

Infact, previous DFT calculations have shown that Co-N_4 centers are indeed energetically more favorable than Co-N_2 centers.[36] These findings are pretty consistent with experiments where graphitic Co-N_4 defects are expected to dominate in catalysts that are synthesized at low pyrolysis temperatures.[1] Moreover, graphitic Co-N_4 defects are predicted to be stable (exothermic formation energy) for potentials in the range $U = 0 - 1.23$ V while the stability of Co-N_2 defects is limited to potentials below 0.45 V. Experimental studies have also shown that Co-N_4 defects are present even at high pyrolysis temperatures.[69] These measurements suggest that Co-N_4 is the dominant catalytically active graphitic defect motif in Co–N_x/C electrocatalysts. O_2 reacts with both types of graphitic Co-N_x ($x = 2, 4$) defects and the presence of either or both defects will enhance at least the reduction of O_2 to peroxide. However, experimental data suggests that Co-N_4 does not interact very strongly with hydrogen peroxide. Thus, a second site for the reduction of peroxide is required, supporting a $2x2e^-$ dual site ORR pathway in both alkaline and acidic electrolyte.

In contrast, the much stronger interaction of Co-N_2 with peroxide supports a $2x2e^-$ single site ORR mechanism, independent of pH. However, the results show that even though this defect may be present after pyrolysis, it may not be stable at relevant fuel cell potentials. Thus, Co-N_2 defects may be present in the as-prepared catalyst, but may comparatively easily corrode, leading to morphological changes of the catalyst. Simultaneously, previous computations predict that the ORR pathway changes from single Co-N_2 + dual Co-N_4 site ORR mechanism to a dual site mechanism as Co defects dissolve into the electrolyte under fuel cell operating conditions.[1]

In the case of Fe-N_2 configurations, the binding energy is generally lower than that in Fe-N_4 configurations. In the case of Fe-N_4 configurations, theoretical results show that the pyridinic (6 ring) configurations are energetically preferred over pyrrolic (5 ring) configurations (Fig 42). The results also favor incorporation of Fe-N_4 sites. [24]
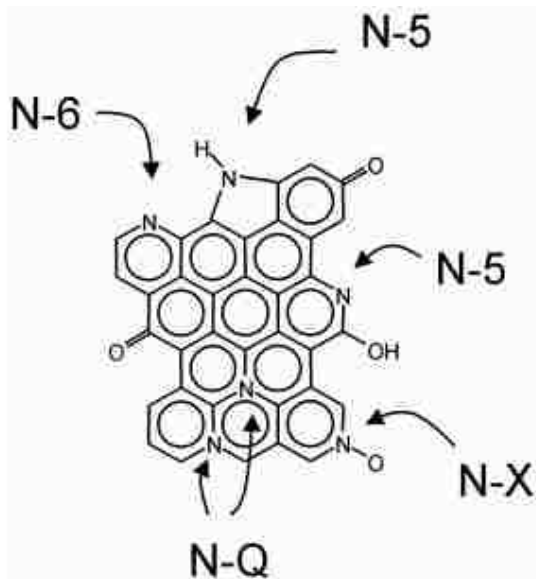

Fig 42: Nitrogen-containing functional groups in activated carbon. N-6: pyridine-like structures, N-5: pyrrolic and/or pyridon-N moieties, N-Q: quaternary nitrogen, N-X: N-oxides. [91]

Interestingly, we note that Fe-N_4 defect has a similar N1s core level shift of 1.5 eV to that of Fe-N_3. Thus, both defects are expected to appear in close proximity in XPS spectra suggesting that the correlation of spectral features and defect chemistry/geometry remains difficult. However, additional correlation can be provided using Fe2p or C1s core level shifts. The overall N1s trend is as follows : Fe-N_3 ~ Fe-N_4 > Fe-N_2. This suggests that it is easier to correlate defect geometry and CLS core level shifts in Co-N_x in particular it may be possible to identify Co-N_3.

Additional Correlation for Fe-N$_3$ and Fe-N$_4$: C1s and TM-2p

C1s shifts

A difficulty for the comparison of core-level binding energies with experiment is that density functional theory is not sufficiently accurate to determine absolute values for orbital binding energies. Using C1s as internal calibration standard may result in as large as 1 eV difference in calibration shift as compared to a Au 4f standard.[36] The difference between positions of pyrrolic and pyridinic N is also about 1 eV. Using C as internal calibration standard, thus, may cause misidentification of N species and thus, may result in significant differences in the derived relative distribution of the pyrrolic vs. pyridinic type of N.

CLS for TM-2p

The binding energies of TM2p orbitals are more challenging to compute since we only account for the average shift of 2p1/2 and 2p3/2 orbitals. This systematic behavior is explained by taking into consideration the splitting of the d-band of the transition metal in this kind of complexes. [25] Thus, the 2p core level shifts are less reliable since the two involved orbitals may shift differently. The origin of the differences between the TM-2p core level shifts and experimental observations remains unclear. The computations provide an average CLS over multiplet splitting which may not be representative for orbital specific CLS which could explain the difference.

Alternatively, the 3-d orbital ordering may be incorrect. This latter option was tested by including a Hubbard+U term in the computations. This term essentially introduces an energetic "penalty" for double occupation of orbitals, thereby affecting the magnetic structure of the transition metal.

Preliminary results show that magnetism at least in Fe-N_4 remains unaffected, likely due to strong orbital pinning through nitrogen 2p Fe 3d interactions. Indirectly, this observation suggests that the orbital ordering remains unaffected and by inference that the charge density at the Fe nucleus does not change, hence the CLS is expected to remain unaffected. In summary, TM-2p CLS remain significantly more challenging as compared to 1s CLS.

Tests for FeN_4-C_{26} show that a denser k-point sampling changes CLS by less 0.01 eV for Fe2p. Tests with different C and N potentials reveal that CLS are expected to be accurate to within 0.2 eV for N1s and 0.1 eV for Fe-2p.

Nevertheless, there is almost a perfect correlation: N1s shifts to more positive binding energies while TM-2p shifts to less positive binding energies. The only exception is Co(2p)-N_4 which is predicted to be shifted up not down. This unexpected result has been checked using different algorithms but it persisted. Taking the present results, suggests that Co-2p can be correlated with N1s to fingerprint Co-N_x defects. Similarly, the correlation of N1s and Fe2p may allow us to identify the Fe-N_x defects.

While the DFT predicted Fe2p binding energy for Fe-N_3 has a core level shift of 1.0 eV, Fe-N_4 has shift of 0.3 eV. Although the upward shift of these defects do not compare with that obtained experimentally, the difference between the CLS: (1.0 - 0.3) eV = 0.7 eV, might help resolve the XPS spectra and correctly identify the motifs.

N1s = 1.5 eV	Fe-N$_3$	Fe-N$_4$
CLS (Fe2p) eV	1.0	0.3
Magnetism	3.1	2.0

Table 14: CLS and magnetic moments for Fe-N$_3$ and Fe-N$_4$ defects

An additional correlation can also be provided using Mössbauer spectroscopy. Fe-N$_3$ has a higher magnetic moment as compared to Fe-N$_4$ (Table 14). This difference in magnetism combined with the core level shift data could be combined with first-principles calculations to facilitate structural analysis for illustrating how binding energy calculations can help elucidate catalyst structures. In conclusion, the DFT core level shift computations show that 1s shifts especially for N1s correlate well with experimental observations. Thus, computed core level shifts can be used to deconvolute XPS spectra. In contrast, the TM-2p computations while internally consistent are at variance with experimental expectations based on cross-correlations between ORR and XPS observation.
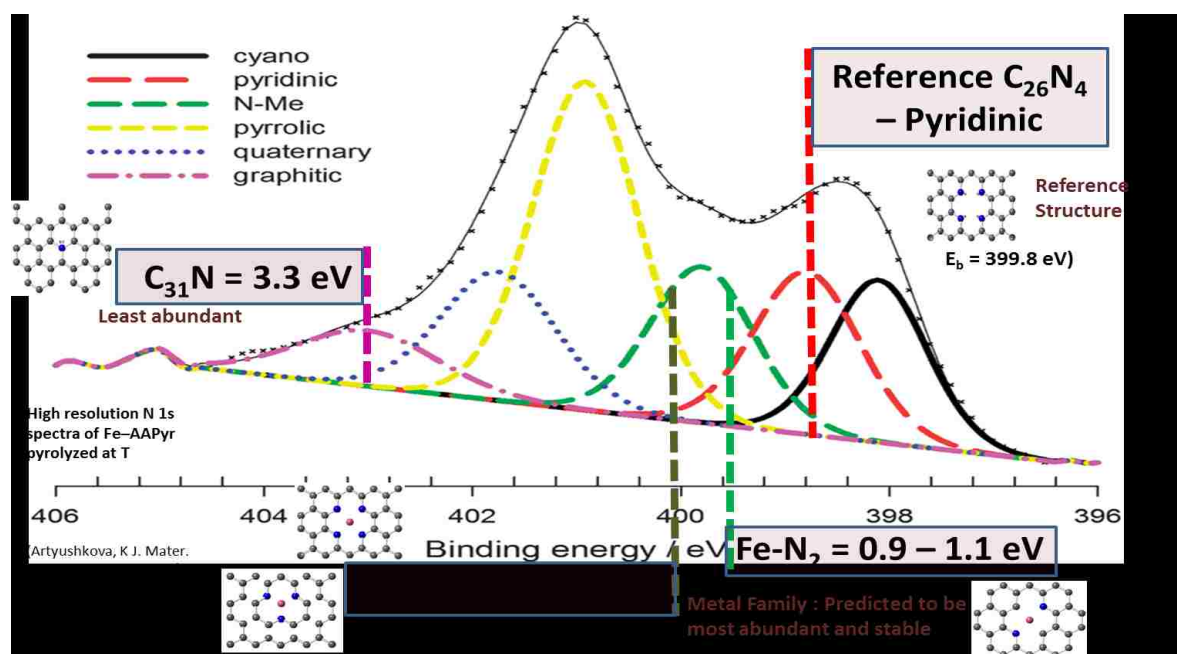

Fig 43 : Predicted DFT core level shifts of Fe-N$_x$ motifs

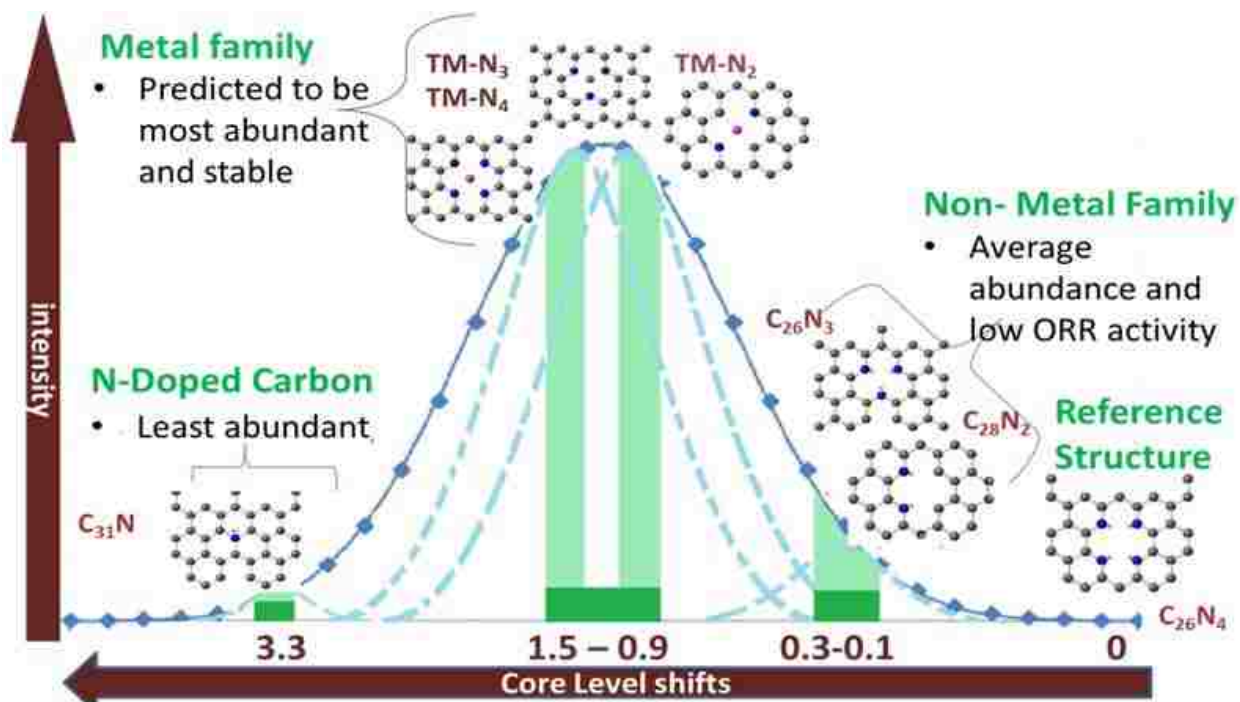**Summary of DFT Predicted Core Level Shifts for TM-N$_x$ Defects**:

Fig 44 : Abundance and Core Level Shifts of TM-N$_x$/C ORR Electrocatalyst

- Metal free (CN$_x$) defects are predicted to have a CLS range of 0.1-0.3 eV, average abundance and ORR activity.

- TM-N$_x$ defects range from 0.9 to 1.5 eV

- TM-N$_2$ – 0.9-1.1eV, high abundance. Not very stable at high potentials

- TM-N$_3$ and TM-N$_4$ defects : CLS 1.3-1.5 eV – highest abundance and most ORR active and energetically favorable and stable at all potentials when compared to TM-N$_2$

- C$_{31}$N : CLS 3.3 eV, low abundance, therefore unlikely to be present in operating conditions

- Fe-N$_3$ and Fe-N$_4$ have similar CLS. Can be distinguished using Fe2p correlation and magnetic moments.
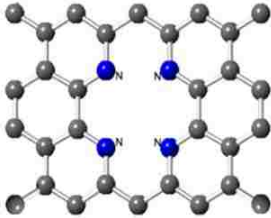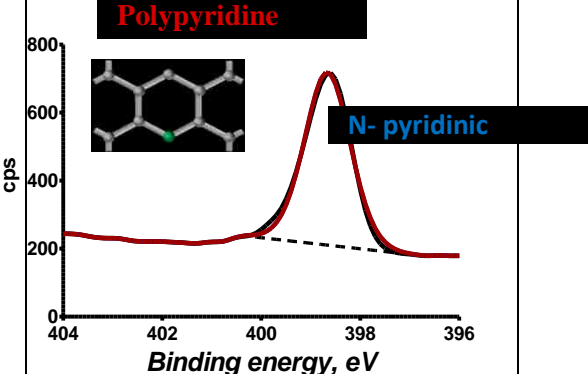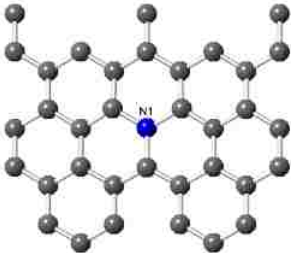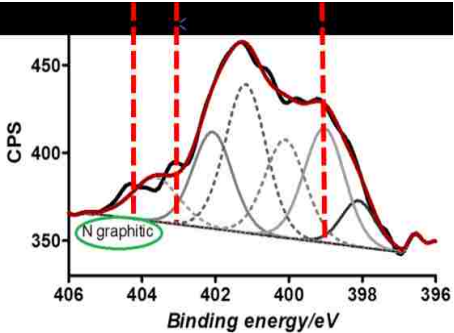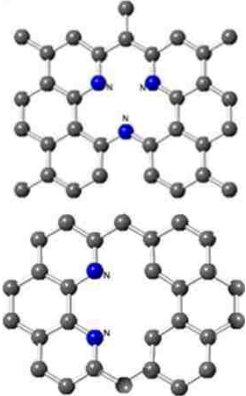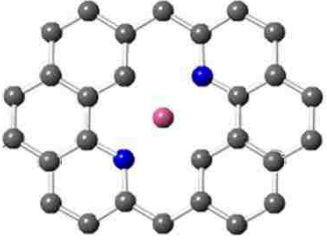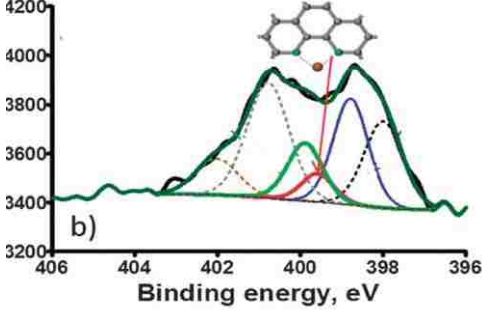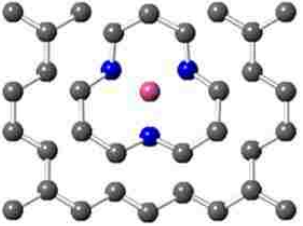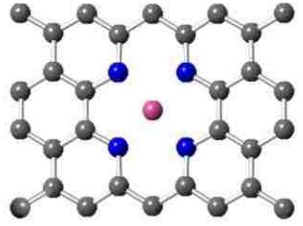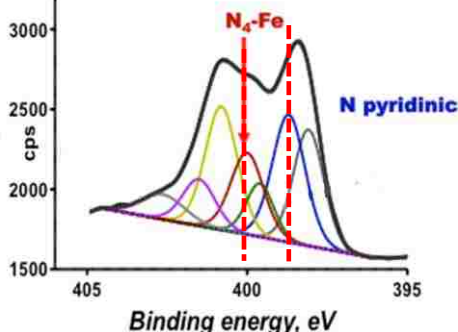
Defect	DFT : N1s core level shift (eV)	Experimental : XPS Spectra
$C_{26}N_4$	**CLS =0** (Reference Structure)	N-Pyridinic – Reference Material
$C_{31}N$	**3.3 eV** - ORR active at low potentials - Might corrode away with time due to energetic instability	**3.0 – 4.0 eV**
$C_{26}N_3$ and $C_{28}N_2$	**0.1 – 0.3 eV** - Average abundance - Limited ORR activity	- **NA**

Table 15 : Summary of DFT vs. XPS core level shifts

Defect	DFT : N1s Core level shift (eV)	XPS : Experimental shift
TMN$_2$-C$_{28}$	**Fe-N$_2$ = 0.9 – 1.1 eV** **Co-N$_2$ = 0.8 – 1.1 eV** -Average abundance -Unstable at high potentials	**Fe-N$_2$ = NA** **Co-N$_2$ = 0.9 – 1.1 eV**
TMN$_3$-C$_{26}$	**Fe-N$_3$ = 1.5 eV** **Co-N$_3$ = 1.5 eV** -Highest ORR activity -Most stable -Fe-N$_3$ and Fe-N4 are indistinguishable -need additional correlation	**Fe-N$_3$ = NA** **Co-N$_3$ = NA**
TMN$_4$-C$_{26}$	**Fe-N$_4$ = 1.5 eV** **Co-N$_4$ = 1.3 eV**	**Fe-N$_4$ = 1.1 eV** **Co-N$_4$ = NA**

Conclusion

The research results presented in this thesis combines theoretical and experimental techniques to analyze and interpret XPS and illustrate that DFT calculations can aid in designing non-PGM electrocatalysts for fuel cells. We have demonstrated for the first time the use of independent DFT predicted binding energy shifts for defect identification and constraining XPS observations for TM–N_x moieties in pyrolyzed Carbon based ORR electrocatalysts. DFT first-principle *ab-initio* calculations were used to predict N1s, Fe2p and Co2p orbitals binding energies for a number of candidate defect motifs which were also characterized using XPS.

Our study shows that the accuracy of DFT core level shifts calculations compares favorably with conventional XPS and to predict core level shift which is expected to be invaluable for the derivation of ORR-activity/defect motif correlations. Our calculations compared very favorably with the experimental results, especially for the Co-N_x defects. The Fe-N_x defects had a few minor deviations, but the precision provided with DFT calculations was estimated to be ~20 meV which is much lower when compared to the 101 meV resolution of synchrotron-based XPS and the 500 meV resolution of conventional XPS

The DFT predicted shifts suggests correlations between N1s, and Fe-2p that may allow us to identify uniquely the defect motifs in a non-PGM electrocatalyst, in the template, the as-prepared catalyst, and after operation. Core level shifts have been used to analyze the surface structure and predict the nature of the surface species in catalysis.

The proposed combination of XPS and core-level binding energy calculations provides us with a new and powerful technique to investigate the structure of surface species and to help identify the nature of TM-N_x defect moieties. However, to fully elucidate catalyst structures and characterize the materials, it is important to point out that this approach should also be combined with an arsenal of complementary techniques such as X-ray-based characterization techniques, vibrational spectroscopies, Mössbauer spectroscopy analysis of the Fe-2p transition metal orbitals As the research presented here shows, the synergy of experiment and theory allows extracting key material parameters for establishing structure/property relationships which are needed for the rational design of novel electrocatalysts for ORR activity and provides us with a unique platform for engineering cost efficient high performance Non-PGM electrocatalysts catalysts for PEM Fuel cells.

References

(1)   Kattel, S.; Atanassov, P.; Kiefer, B. *Phys Chem Chem Phys* **2013**, *15*, 148.

(2)   Greeley, J.; Stephens, I. E. L.; Bondarenko, A. S.; Johansson, T. P.; Hansen, H. A.; Jaramillo, T. F.; Rossmeisl, J.; Chorkendorff, I.; Norskov, J. K. *Nat Chem* **2009**, *1*, 552.

(3)   Wagner, F. T.; Lakshmanan, B.; Mathias, M. F. *J Phys Chem Lett* **2010**, *1*, 2204.

(4)   Thomas, C. E. *Int J Hydrogen Energ* **2009**, *34*, 6005.

(5)   Bezerra, C. W. B.; Zhang, L.; Lee, K. C.; Liu, H. S.; Marques, A. L. B.; Marques, E. P.; Wang, H. J.; Zhang, J. J. *Electrochim Acta* **2008**, *53*, 4937.

(6)   Zhang, L.; Zhang, J. J.; Wilkinson, D. P.; Wang, H. J. *J Power Sources* **2006**, *156*, 171.

(7)   Othman, R.; Dicks, A. L.; Zhu, Z. H. *Int J Hydrogen Energ* **2012**, *37*, 357.

(8)   Feng, Y. J.; Alonso-Vante, N. *Physica Status Solidi B-Basic Solid State Physics* **2008**, *245*, 1792.

(9)   Srinivasan, S. *Abstr Pap Am Chem S* **1988**, *195*, 279.

(10)   Arico, A. S.; Srinivasan, S.; Antonucci, V. *Fuel Cells* **2001**, *1*, 133.

(11)   Steele, B. C. H.; Heinzel, A. *Nature* **2001**, *414*, 345.

(12)   Kramm, U. I.; Herranz, J.; Larouche, N.; Arruda, T. M.; Lefevre, M.; Jaouen, F.; Bogdanoff, P.; Fiechter, S.; Abs-Wurmbach, I.; Mukerjee, S.; Dodelet, J. P. *Phys Chem Chem Phys* **2012**, *14*, 11673.

(13)   Gasteiger, H. A.; Kocha, S. S.; Sompalli, B.; Wagner, F. T. *Appl Catal B-Environ* **2005**, *56*, 9.

(14)   Baglio, V.; Arico, A. S.; Stassi, A.; D'Urso, C.; Di Blasi, A.; Luna, A. M. C.; Antonucci, V. *J Power Sources* **2006**, *159*, 900.

(15)   Bashyam, R.; Zelenay, P. *Nature* **2006**, *443*, 63.

(16)   Karim, N. A.; Kamarudin, S. K. *Appl Energ* **2013**, *103*, 212.

(17)   Kruusenberg, I.; Matisen, L.; Shah, Q.; Kannan, A. M.; Tammeveski, K. *Int J Hydrogen Energ* **2012**, *37*, 4406.

(18)   Ma, Y. W.; Zhang, H. M.; Zhong, H. X.; Xu, T.; Jin, H.; Tang, Y. F.; Xu, Z. A. *Electrochim Acta* **2010**, *55*, 7945.

(19)   Feng, Y. X.; Yao, X. L.; Wang, M.; Hu, Z. P.; Luo, X. G.; Wang, H. T.; Zhang, L. X. *J Chem Phys* **2013**, *138*.

(20)   Geim, A. K.; Novoselov, K. S. *Nat Mater* **2007**, *6*, 183.

(21)   Proietti, E.; Jaouen, F.; Lefevre, M.; Larouche, N.; Tian, J.; Herranz, J.; Dodelet, J. P. *Nat Commun* **2011**, *2*.

(22)   Lee, K.; Zhang, L.; Zhang, J. J. *J Power Sources* **2007**, *170*, 291.

(23)   Ohms, D.; Herzog, S.; Franke, R.; Neumann, V.; Wiesener, K.; Gamburcev, S.; Kaisheva, A.; Iliev, I. *J Power Sources* **1992**, *38*, 327.

(24)   Titov, A.; Zapol, P.; Kral, P.; Liu, D. J.; Iddir, H.; Baishya, K.; Curtiss, L. A. *J Phys Chem C* **2009**, *113*, 21629.

(25)   Calle-Vallejo, F.; Martinez, J. I.; Rossmeisl, J. *Phys Chem Chem Phys* **2011**, *13*, 15639.

(26)   Gouerec, P.; Savy, M. *Electrochim Acta* **1999**, *44*, 2653.

(27)   Kalvelage, H.; Mecklenburg, A.; Kunz, U.; Hoffmann, U. *Chem Eng Technol* **2000**, *23*, 803.

(28)   Meng, H.; Jaouen, F.; Proietti, E.; Lefevre, M.; Dodelet, J. P. *Electrochem Commun* **2009**, *11*, 1986.

(29)   Medard, C.; Lefevre, M.; Dodelet, J. P.; Jaouen, F.; Lindbergh, G. *Electrochim Acta* **2006**, *51*, 3202.

(30)   Kattel, S.; Atanassov, P.; Kiefer, B. *J Phys Chem C* **2012**, *116*, 17378.

(31)   Mustain, W. E.; Prakash, J. *J Power Sources* **2007**, *170*, 28.

(32)   Olson, T. S.; Pylypenko, S.; Fulghum, J. E.; Atanassov, P. *J Electrochem Soc* **2010**, *157*, B54.

(33)   Matter, P. H.; Ozkan, U. S. *Catal Lett* **2006**, *109*, 115.

(34)   Matter, P. H.; Zhang, L.; Ozkan, U. S. *J Catal* **2006**, *239*, 83.

(35)   Maldonado, S.; Stevenson, K. J. *J Phys Chem B* **2004**, *108*, 11375.

(36)   Artyushkova, K.; Kiefer, B.; Halevi, B.; Knop-Gericke, A.; Schlogl, R.; Atanassov, P. *Chem Commun* **2013**, *49*, 2539.

(37)   Liu, G.; Li, X. G.; Ganesan, P.; Popov, B. N. *Appl Catal B-Environ* **2009**, *93*, 156.

(38)   Lefevre, M.; Dodelet, J. P.; Bertrand, P. *J Phys Chem B* **2002**, *106*, 8705.

(39)   Biloul, A.; Contamin, O.; Scarbeck, G.; Savy, M.; Vandenham, D.; Riga, J.; Verbist, J. J. *J Electroanal Chem* **1992**, *335*, 163.

(40)   Kramm, U. I.; Herrmann-Geppert, I.; Bogdanoff, P.; Fiechter, S. *J Phys Chem C* **2011**, *115*, 23417.

(41)   Tian, J.; Birry, L.; Jaouen, F.; Dodelet, J. P. *Electrochim Acta* **2011**, *56*, 3276.

(42)   Jaouen, F.; Dodelet, J. P. *J Phys Chem C* **2007**, *111*, 5963.

(43)   Wu, G.; More, K. L.; Xu, P.; Wang, H. L.; Ferrandon, M.; Kropf, A. J.; Myers, D. J.; Ma, S. G.; Johnston, C. M.; Zelenay, P. *Chem Commun* **2013**, *49*, 3291.

(44)   van Mourik, T.; Gdanitz, R. J. *J Chem Phys* **2002**, *116*, 9620.

(45)   Kohn, W.; Becke, A. D.; Parr, R. G. *J Phys Chem-Us* **1996**, *100*, 12974.

(46)   Argaman, N.; Makov, G. *Am J Phys* **2000**, *68*, 69.

(47)   Kohn, W. *Rev Mod Phys* **1999**, *71*, 1253.

(48)   Schrodinger, E. *Phys Rev* **1926**, *28*, 1049.

(49)   Connor, J. N. L.; Uzer, T.; Marcus, R. A.; Smith, A. D. *J Chem Phys* **1984**, *80*, 5095.

(50)   Kato, T. *T Am Math Soc* **1951**, *70*, 195.

(51)   VI, A.; Aryasetiawan, F.; Lichtenstein, A. I. *J Phys-Condens Mat* **1997**, *9*, 767.

(52)   Kohn, W.; Sham, L. J. *Phys Rev* **1965**, *140*, 1133.

(53)   Kohn, W.; Sham, L. J. *Phys Rev* **1965**, *137*, 1697.

(54)   Lang, N. D.; Kohn, W. *Phys Rev B* **1970**, *1*, 4555.

(55)   Langreth, D. C.; Perdew, J. P. *Phys Rev B* **1977**, *15*, 2884.

(56)   Burke, K.; Perdew, J. P.; Ernzerhof, M. *Int J Quantum Chem* **1997**, *61*, 287.

(57)   Paier, J.; Marsman, M.; Hummer, K.; Kresse, G.; Gerber, I. C.; Angyan, J. G. *J Chem Phys* **2006**, *125*.

(58)   Hohenberg, P.; Kohn, W. *Phys Rev B* **1964**, *136*, B864.

(59)   Vosko, S. H.; Wilk, L.; Nusair, M. *Can J Phys* **1980**, *58*, 1200.

(60)   Kresse, G.; Furthmuller, J. *Phys Rev B* **1996**, *54*, 11169.

(61)   Kohler, L.; Kresse, G. *Phys Rev B* **2004**, *70*.

(62)   Blochl, P. E. *Phys Rev B* **1994**, *50*, 17953.

(63)   Perdew, J. P.; Burke, K.; Ernzerhof, M. *Phys Rev Lett* **1996**, *77*, 3865.

(64)   Monkhorst, H. J.; Pack, J. D. *Phys Rev B* **1976**, *13*, 5188.

(65)   Kattel, S.; Atanassov, P.; Kiefer, B. *J Phys Chem C* **2012**, *116*, 8161.

(66)   Pasanen, P.; Voutilainen, M.; Helle, M.; Song, X. F.; Hakonen, P. *J Phys Scripta* **2012**, *T146*.

(67)   Shao, Y. Y.; Zhang, S.; Engelhard, M. H.; Li, G. S.; Shao, G. C.; Wang, Y.; Liu, J.; Aksay, I. A.; Lin, Y. H. *J Mater Chem* **2010**, *20*, 7491.

(68)   Kannan, P.; Maiyalagan, T.; Sahoo, N. G.; Opallo, M. *J Mater Chem B* **2013**, *1*, 4655.

(69)   Bouwkamp-Wijnoltz, A. L.; Visscher, W.; van Veen, J. A. R.; Boellaard, E.; van der Kraan, A. M.; Tang, S. C. *J Phys Chem B* **2002**, *106*, 12993.

(70)   Turner, S.; Egoavil, R.; Batuk, M.; Abakumov, A. A.; Hadermann, J.; Verbeeck, J.; Van Tendeloo, G. *Appl Phys Lett* **2012**, *101*.

(71)   Collman, J. P.; Gagne, R. R. *Abstr Pap Am Chem S* **1974**, 31.

(72)   Knop-Gericke, A.; Kleimenov, E.; Havecker, M.; Blume, R.; Teschner, D.; Zafeiratos, S.; Schlogl, R.; Bukhtiyarov, V. I.; Kaichev, V. V.; Prosvirin, I. P.; Nizovskii, A. I.; Bluhm, H.; Barinov, A.; Dudin, P.; Kiskinova, M. *Adv Catal* **2009**, *52*, 213.

(73)   Nordling, C.; Sokolowski, E.; Siegbahn, K. *Phys Rev* **1957**, *105*, 1676.

(74)   Trinh, Q. T.; Tan, K. F.; Borgna, A.; Saeys, M. *J Phys Chem C* **2013**, *117*, 1684.

(75)   Powell, C. J.; Jablonski, A.; Tilinin, I. S.; Tanuma, S.; Penn, D. R. *J Electron Spectrosc* **1999**, *98*, 1.

(76)   Powell, C. J.; Jablonski, A. *Nucl Instrum Meth A* **2009**, *601*, 54.

(77)   Weinert, M.; Watson, R. E. *Phys Rev B* **1995**, *51*, 17168.

(78)   Chauveau, D.; Roubin, P.; Guillot, C.; Lecante, J.; Treglia, G.; Desjonqueres, M. C.; Spanjaard, D. *Solid State Commun* **1984**, *52*, 635.

(79)   Robson, M. H.; Serov, A.; Artyushkova, K.; Atanassov, P. *Electrochim Acta* **2013**, *90*, 656.

(80)   Nelin, C. J.; Bagus, P. S.; Ilton, E. S.; Chambers, S. A.; Kuhlenbeck, H.; Freund, H. J. *Int J Quantum Chem* **2010**, *110*, 2752.

(81)   Bagus, P. S.; Illas, F.; Pacchioni, G.; Parmigiani, F. *J Electron Spectrosc* **1999**, *100*, 215.

(82)   Norskov, J. K.; Bligaard, T.; Rossmeisl, J.; Christensen, C. H. *Nat Chem* **2009**, *1*, 37.

(83)   Nilsson, A.; Bennich, P.; Wiell, T.; Wassdahl, N.; Martensson, N.; Nordgren, J.; Bjorneholm, O.; Stohr, J. *Phys Rev B* **1995**, *51*, 10244.

(84)   Olovsson, W.; Goransson, C.; Marten, T.; Abrikosov, I. A. *Physica Status Solidi B-Basic Solid State Physics* **2006**, *243*, 2447.

(85)   Bagus, P. S.; Freund, H. J.; Minerva, T.; Pacchioni, G.; Parmigiani, F. *Chem Phys Lett* **1996**, *251*, 90.

(86)   Richter, B.; Kuhlenbeck, H.; Freund, H. J.; Bagus, P. S. *Phys Rev Lett* **2004**, *93*.

(87)   Takahata, Y.; Marques, A. D. *J Electron Spectrosc* **2010**, *178*, 80.

(88)   Sham, L. J.; Kohn, W. *Phys Rev* **1966**, *145*, 561.

(89)   Sidik, R. A.; Anderson, A. B.; Subramanian, N. P.; Kumaraguru, S. P.; Popov, B. N. *J Phys Chem B* **2006**, *110*, 1787.

(90)   Xu, J.; Shen, K.; Xue, B.; Li, Y. X. *J Mol Catal a-Chem* **2013**, *372*, 105.

(91)   Kapteijn, F.; Moulijn, J. A.; Matzner, S.; Boehm, H. P. *Carbon* **1999**, *37*, 1143.